

INFORMATION TO USERS

This material was produced from a microfilm copy of the original document. While the most advanced technological means to photograph and reproduce this document have been used, the quality is heavily dependent upon the quality of the original submitted.

The following explanation of techniques is provided to help you understand markings or patterns which may appear on this reproduction.

1. The sign or "target" for pages apparently lacking from the document photographed is "Missing Page(s)". If it was possible to obtain the missing page(s) or section, they are spliced into the film along with adjacent pages. This may have necessitated cutting thru an image and duplicating adjacent pages to insure you complete continuity.
2. When an image on the film is obliterated with a large round black mark, it is an indication that the photographer suspected that the copy may have moved during exposure and thus cause a blurred image. You will find a good image of the page in the adjacent frame.
3. When a map, drawing or chart, etc., was part of the material being photographed the photographer followed a definite method in "sectioning" the material. It is customary to begin photoing at the upper left hand corner of a large sheet and to continue photoing from left to right in equal sections with a small overlap. If necessary, sectioning is continued again – beginning below the first row and continuing on until complete.
4. The majority of users indicate that the textual content is of greatest value, however, a somewhat higher quality reproduction could be made from "photographs" if essential to the understanding of the dissertation. Silver prints of "photographs" may be ordered at additional charge by writing the Order Department, giving the catalog number, title, author and specific pages you wish reproduced.
5. PLEASE NOTE: Some pages may have indistinct print. Filmed as received.

University Microfilms International

300 North Zeeb Road
Ann Arbor, Michigan 48106 USA
St. John's Road, Tyler's Green
High Wycombe, Bucks, England HP10 8HR

77-25,974

CHANG, Chung-Ping, 1943-
THE DISLOCATION MORPHOLOGY IN
DEFORMED AND IRRADIATED NIOBIUM.

Iowa State University, Ph.D., 1977
Engineering, metallurgy

Xerox University Microfilms, Ann Arbor, Michigan 48106

The dislocation morphology in deformed
and irradiated niobium

by

Chung-Ping Chang

A Dissertation Submitted to the
Graduate Faculty in Partial Fulfillment of
The Requirements for the Degree of
DOCTOR OF PHILOSOPHY

Department: Materials Science and Engineering

Major: Metallurgy

Approved:

Signature was redacted for privacy.

In Charge of Major Work

Signature was redacted for privacy.

For the Major Department

Signature was redacted for privacy.

For the Graduate College

Iowa State University
Ames, Iowa

1977

TABLE OF CONTENTS

	Page
INTRODUCTION	1
Dissociation of Glissile Dislocations	2
Interactions between Dislocations	3
Damage Structure of the As-Irradiated and Irradiated-Annealed bcc Metals	5
Objectives of the Study	8
EXPERIMENTAL PROCEDURE	11
Specimen Preparation	11
Tensile Straining	11
Irradiation and Post-Irradiation Annealing	13
Electrom Microscopy	13
RESULTS AND DISCUSSION	16
Dislocation Dissociation	16
TEM evidence	16
Stacking fault energy	30
Dislocation Interactions	33
Interactions between two glissile dislocations	33
Interactions between dislocation loops and dislocations in a group	38
Energy of interaction	51
Irradiated and Irradiated-Annealed Niobium	55
Damage structure at the as-irradiated Nb	55
Damage structure after annealing	65
Defect production	83
Defect clusters	87
Annealing mechanisms	94
SUMMARY	100
REFERENCES	102
ACKNOWLEDGMENTS	108

INTRODUCTION

Scientific studies on the mechanical behavior of all body-centered cubic (bcc) metals except the indispensable iron were comparatively rare until the 1960's. Since then, an increasing number of experimental studies have been carried out on plasticity, point defects and radiation damage in bcc metals. The growing interest in the bcc refractory metals (V, Cr, Nb, Mo, Ta and W) was largely generated by the potential of various applications at high temperatures or for the construction of advanced reactors, and by the desire for a better understanding of this important group of transition metals.

The information furnished by recent investigations on bcc metals has rapidly narrowed the knowledge gap between face-centered cubic (fcc) and bcc metals. Still information for bcc metals is far from complete on such important properties as the dissociation of glissile dislocations, the effect of impurities, the interactions between dislocations and the behavior of point defects.

The present study deals with three aspects of the morphology of dislocations in Nb: (1) the dissociation of dislocations (2) the interactions between glissile dislocations and (3) the damage structure induced by fast neutrons and its annealing behavior. Interstitial impurities are known to exert pronounced effects on properties of bcc metals. Numer-

ous studies have been conducted on various bcc metals by a variety of methods (1-8). For this reason, the effect of interstitial impurity was not included in the present study.

Dissociation of Glissile Dislocations

The formation of the extended dislocations and their associated stacking faults in metals have been well recognized since the proposed dissociation of unit dislocations in the fcc crystals by Heidenreich and Shockley (9). Indeed, transmission electron microscopy (TEM) evidence has been obtained for the existence of partial dislocations in pairs connected by stacking faults in fcc, hcp (hexagonal close-packed) and diamond structures (10-12). TEM evidence of extended dislocations in bcc metals did not emerge until 1975 (13). Despite the absence of direct evidence for the existence of stacking faults in bcc metals, the dissociated core model is capable of explaining many features of plasticity, such as slip asymmetry (14-17), the predominance of straight screw dislocations in crystals deformed at low temperatures (18) and the temperature dependence of flow stress (19-21).

Controversy over the existence of stacking faults in bcc metals has been discussed extensively in the literature. Several workers (21-31) performed theoretical analyses on the core structure of dislocations. Because of the uncertainty concerning (1) the mode and the extent of elastic relaxation, (2) the atomic potential and (3) the cut-off distance of

interactions, no agreement has been reached on the stability of partial dislocations. Moreover, all theoretical calculations were based on atomic potentials which may be justified for simple bcc metals such as sodium, but certainly not for transition metals. In the meantime numerous studies have been conducted to search for "pure" stacking faults associated with extended dissociations in Nb (32-34), Fe (35), W (36) and Cr (37). According to Christian (38), however, all TEM observations of the fringe-type contrast on the {112} and {123} planes up to the time of this review had been complicated by impurity atoms. The same author also disputed the field-ion microscopy (FIM) evidence reported for the dissociation of dislocations in W and Fe by Smith et al. (39,40) for the reason that the large electrostatic field acting on the surface of the specimen can generate a hydrostatic tension at the tip, thereby extraneously stabilizing the enclosed stacking faults (41). Christian's remarks reflect the concensus that clear-cut evidence for dissociated dislocations and stacking faults in bcc metals has not been established up to 1975.

Interactions between Dislocations

Up to date TEM investigations (42,43) have shown that glissile dislocations in bcc metals are primarily of the $(a/2)\langle 111 \rangle$ type, with some of the $\langle 001 \rangle$ type. The $a\langle 110 \rangle$ dislocations were only observed (44) as a result of a repulsive cutting between two $(a/2)\langle 111 \rangle$ dislocations.

Glissile dislocations in crystalline solids have long been known to be highly versatile, as reflected by the complex behavior of plastic deformation and fracture of metals. To a large extent, this versatility stems from the great probability and ease with which moving dislocation will encounter other dislocations, thus interacting to yield new dislocations. In theory, the only requirement for two or more meeting dislocations to interact is a reduction in energy; that is,

$$\Delta E = \sum^p E_p - \sum^r E_r < 0, \quad (1)$$

where E_p and E_r are the self-energies of the product and reactant dislocations, respectively. For a straight dislocation, the self-energy per unit length is given by Bullough and Foreman (45),

$$E = \frac{Gb^2}{4\pi(1-\nu)} \left[(1-\nu \cos^2 \alpha) \ln\left(\frac{R}{r_0}\right) - \frac{\sin^2 \alpha (3-4\nu)}{4(1-\nu)} \right], \quad (2)$$

where G is the shear modulus, b the magnitude of the Burgers vector, R the outer bound of the strain-energy integration, r_0 the core radius, α the angle between the line direction and the Burgers vector, and ν Poisson's ratio. Numerous interactions have been proposed for bcc metals. Little success has been attained in the attempts to confirm the proposed interactions of dislocations by TEM, however.

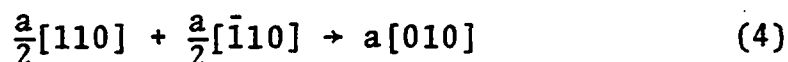
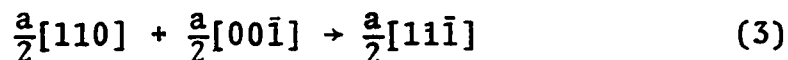
To illustrate the seriousness of the problems, we recall that Hartley (46) cited 12 possible interactions between

$(a/2)\langle 1\bar{1}1 \rangle\{110\}$ glissile dislocations in the bcc metals, including the renowned one $(a/2)[111]_{(\bar{1}01)} + (a/2)[\bar{1}\bar{1}\bar{1}]_{(101)} + a[100]_{(00\bar{1})}$ originally suggested for the generation of incipient $a\langle 100 \rangle$ cracks in the cleavage planes by Cottrell (47). More recently, four other interactions were described by Lindroos (48), which involve more than two $(a/2)\langle 1\bar{1}1 \rangle$ dislocations in the $\{110\}$ planes. A survey of the literature published in the past decade revealed that, of the 16 interactions proposed, only four (Hartley's reactions (2), (3) and (11) quoted in references (49), (50) and (51), respectively and one of Lindroos's (48)) have been confirmed and two others (Hartley's reactions (4) and (10) quoted in references (52) and (53), respectively) might have been established in connection with the initiation of fine twins or cracks.

Damage Structure of the As-Irradiated and Irradiated-Annealed bcc Metals

It is possible to generate a faulted region by condensing a group of point defects to form a Frank-type dislocation loop in a crystalline solid, as has been observed in most of the fcc metals after quenching or irradiation (54). No evidence of quenched-in vacancies has been reported for bcc metals, however. Therefore, the only possible way to produce partial dislocation loops by point-defects condensation is through irradiation. Unlike the dissociation of dislocations, theoretical analysis (55) on the formation of dislocation loops

indicates that faulted loops should be nucleated in the early stages of loop formation in irradiated bcc metals. The faulted loops, however, have the tendency to become perfect loops as a result of shear in two possible directions described by the following reactions:



The perfect loops with $\underline{b} = (a/2)\langle 111 \rangle$ tend to rotate into the $\{111\}$ planes so as to attain a pure edge configuration. Indeed experimental evidence has been shown for the existence of faulted loops in irradiated bcc metals (56).

Another reason for the intensified research in this area is the need for a better understanding of the bcc metals. Despite the steady progress made for fcc metals, our knowledge on the subject is still fragmentary for the bcc metals. The situation has been somewhat improved with Mo as a result of two series of studies by Maher and Eyre (57a,b,c) and by Niebel and Wilkens (58). Valuable information is now available on the nature (vacancy or interstitial), geometry (the Burgers vector and the habit plane), size distribution and number density of defect clusters produced in Mo by fast neutrons with or without subsequent annealing.

Although efforts have also been made for the Group V metals, the results are either contradictory to each other or

only indirectly related to the characteristics of defect clusters. For instance, the existing information on the nature of neutron-induced defect clusters in vanadium shows serious discrepancy. Elen (59) and Rau and Ladd (60) irradiated V of comparable purities to neutron fluences within the same order of magnitude (1 to 7×10^{19} n/cm²) at 50-80°C, followed by annealing at 400-600°C. While Elen found the induced dislocation loops lying on the {111} planes with $\underline{b} = (a/2)\langle 111 \rangle$ and identified them as predominantly of the vacancy type, Rau and Ladd described the defect clusters as "probably" interstitial in nature. In a more recent study, Shiraishi et al. (61) summarized that "upon post-irradiation annealing, vacancy loops grow in the specimens irradiated to 8.2×10^{19} n/cm²" at 140°C "and interstitial loops grow in the specimens irradiated to 4.2×10^{19} n/cm² or less fluences" at 70°C. The latter workers' results hardly explained the conflicting conclusions drawn by Elen and Rau and Ladd.

The problems with niobium in Group Va are different from vanadium. Numerous TEM studies have been conducted on Nb, but the majority of them emphasized the prominent roles played by the defect clusters in radiation-(62-64) and radiation-anneal (65) hardening and in flux pinning (66). Hence attention was paid mainly to the size distribution and number density of defect clusters, leaving the nature and geometry of the clusters much less investigated, Rühle et al. (67) recently made a serious attempt to characterize small ($< 200 \text{ \AA}$) clusters

induced in Nb by fast neutrons. Nb sheets of 99.9% purity were irradiated to 8×10^{17} n/cm² ($E > 0.1$ MeV) at $\sim 80^\circ\text{C}$ and showed for 41 loops a split of 26:15 for a normalized ℓ_V/ℓ_I loop ratio of 1/0.58 in favor of vacancies. The 41 loops had Burgers vectors parallel to the $\langle 100 \rangle$, $\langle 110 \rangle$ and $\langle 111 \rangle$ directions with roughly equal frequency, similar to those reported by Tucker and Ohr (68). The same group (69) later examined 250 loops ranging from 25 to 150 \AA in two Nb specimens irradiated to 6×10^{17} n/cm² at 4.2 and 353°K . The ℓ_V/ℓ_I loop ratio was found to be 1/1.35 and 1/1.86, respectively. The reversal in the loop ratio between their own two studies signifies that the reliability of the determination of the ratio depends upon the statistics of loop characterization. These studies suffered from the relatively low neutron fluences used, which are lower by at least an order of magnitude than those usually required for the evaluation of radiation damage in metals. Information on the nature of defect clusters in the irradiated-and-annealed Nb has not been carefully examined heretofore.

Objectives of the Study

An examination of the pertinent literature reveals that basic information on dislocations in bcc metals is still lacking. To gain a better understanding of dislocations in these metals, it is necessary to study the form and structure, i.e. the morphology, of dislocations under different conditions.

In this endeavor, the TEM techniques are invaluable and essential. The purposes of this study were to investigate the possibility of the dissociation of glissile dislocations, the interaction between dislocations and the production and annealing of point-defect clusters by fast neutrons.

Niobium was chosen as the material of interest for four reasons. First, niobium has the lowest estimated stacking fault energy (see Table 1a). Second, it has moderate solubility for the interstitial impurities (see Table 1b), thus it is capable of dissolving the impurities within reasonable limits. Third, niobium is considered to be a candidate for the vacuum wall of the fusion reactor. Information on the characteristics of dislocations and stacking faults in this metal should be of value and interest to the development of advanced reactors. Finally, niobium has not been studied so extensively as tungsten, molybdenum and vanadium.

Table 1a. Estimated stacking fault energies for bcc refractory metals in ergs/cm^{2a}

Ref.	Nb	V	Ta	Cr	Mo	W	
70	E537	589	942	1100	1450	1860	elastic theory
	S291	303	402	720	839	1010	
39						50	field ion microscopy
71	E150	150	210	380	430	500	elastic model
72	21	26	41.4	53.2	66.i	89.2	surface energy

Table 1b. Interstitial impurity solubility limit (73)

	V	Group 5A Nb	Ta	Cr	Group 6A Mo	W
H	10000	9000	1000	0.1-1	0.1	none
C	1000	100	70	0.1-1	0.1-1	0.1
N	5000	300	1000	0.1	1	0.1
O	3000	1000	200	0.1	1	1

^aE - for edge dislocation; S - for screw dislocation.

EXPERIMENTAL PROCEDURE

Specimen Preparation

Two grades of niobium designated as Nb-A and Nb-B were used as the starting materials. Their major impurities are listed in Table 2a. The arc-melted fingers were cold-rolled into sheets to the final thickness of 0.12 mm. To avoid contamination, they were wrapped in aluminum foils before rolling. The sheets were immersed in a solution of 15 parts HF, 45 parts HCl, 15 parts HNO₃ and 25 parts of H₂O, for the removal of the aluminum wrap, followed by rinsing in methanol. Table 2b lists the conditions under which the cleaned sheets were finally annealed and the interstitial impurities in the annealed samples.

Tensile Straining

Specimen deformation before electrolytic thinning was conducted on a Model TT Instron machine by stretching the foil at a strain rate of $1 \times 10^{-3} \text{ sec}^{-1}$. Special attachments to the cross-head and a pair of specimen grips were constructed and installed to minimize possible bending.

Foils were examined by TEM as soon as possible after deformation to avoid complications caused by strain aging. When the deformed foils could not be examined immediately, they were stored in an evacuated desiccator.

Table 2a. As-received niobium with major impurity contents and sources

Grade	300°K/ 4.2°K	Impurity in wt ppm							Source
		Ta	Ti	W	O	H	N	C	
Nb-A	2000	550	100	-	20	5	7	20	Ames Lab.
Nb-B	unknown	1000	100	-	90	4	87	40	Commercial

Table 2b. Final annealing conditions, designations, and chemical analysis

Designation	Original metal	Temp. in °C	Vacuum in torr		Interstitial impurity in wt ppm			
					O	H	N	C
Nb-A-1	Nb-A	975	5×10^{-7}	wrap in Ta foil inside tube furnace	41	2	4	50
Nb-HT-8	Nb-A	2065	2.5×10^{-7}	dynamic vacuum, self-resistance heating	15	4	3	64
Nb-HT-1	Nb-A	2010	5×10^{-7}	sealed in Ta can, high temperature furnace	199	3	75	10
Nb-HT-2	Nb-B	1850	1×10^{-6}	"	1800	7	91	50
Nb-IRR-1	Nb-B	975	3×10^{-8}	sealed in quartz tube, muffle furnace	128	4	87	40

Irradiation and Post-irradiation Annealing

The neutron irradiation experiment was conducted on Nb-B foils inside the flux converter in the central thimble of the Ames Laboratory Research Reactor. The samples were packed inside an aluminum can filled with high purity helium to ensure good thermal equalization during irradiation. Irradiation temperature was $85 \pm 5^\circ\text{C}$ measured by a thermocouple in the center of the can. A nickel wire was included in the sample package for monitoring the fast neutron flux. Flux determination was made from measurement of the γ -decay of Co^{58} induced in nickel by the $\text{Ni}^{58}(\text{n,p})\text{Co}^{58}$ reaction. The dose rate was determined to be 2.4×10^{13} neutron/cm²-sec ($E > 0.1$ MeV) and the fluence was 8×10^{19} n/cm² ($E > 0.1$ MeV).

Post-irradiation anneals were carried out at temperatures between 350° to 1000°C for an hour. Disc specimens of 3 mm diameter were sealed in quartz tubes in vacuum with residual pressure less than 3×10^{-8} torr and annealed in a muffle furnace at the predetermined temperature.

Electron Microscopy

Specimen disks were thinned by a Buehler double jet polisher using 42-48 volts and current density of about 15 mA/mm². The electrolyte contained 2.5 parts H_2SO_4 and 97.5 parts methanol. The polishing was performed at -65°C so as to minimize the danger of specimen contamination by all gaseous elements, except perhaps hydrogen.

A Hitachi electron microscope, Model HU 11A, was used for the TEM examination. The specimen stage was capable of tilting but featured no eucentric axis of tilting. The weak-beam dark-field (WBDF) technique (74) was used for higher resolution and better contrast whenever necessary and applicable. In practice, this technique employs a reflection vector \underline{g} for which $|s_{\underline{g}}| > 0$, where $s_{\underline{g}}$ is the deviation parameter in the kinematical theory of electron diffraction. Since the image intensity is extremely weak under WBDF conditions, focusing was generally difficult and longer exposure time (10 to 30 sec) was required. Despite the shortcomings, this technique proved to be advantageous in several cases and furnished valuable information.

The nature of the dislocation loops was determined by observing the change in image size upon the reversal of the sign of $(\underline{g} \cdot \underline{b})s$ (75). In this endeavor, appropriate $\langle 110 \rangle$ reflections were most frequently used for dislocation loops with $\underline{b} = (a/2)\langle 111 \rangle$, and the change in sign of $(\underline{g} \cdot \underline{b})s$ is accomplished by reversing either \underline{g} or s . Partly because of the relatively low resolution ($\sim 25 \text{ \AA}$) attainable in our microscope, this method of determining the loop nature was found effective only when the loops are larger than $\sim 160 \text{ \AA}$. Consequently, the statistics of the analysis on the loop nature were limited by the number of large-size loops present in the foils. A Zeiss particle-size analyzer was used to determine

the size distribution of defect clusters. To calculate the number density of clusters, an average foil thickness of 1500 Å was assumed, which is subject to $\pm 30\%$ uncertainty. The gross experimental error in the determination of ρ is estimated to be $\pm 50\%$.

RESULTS AND DISCUSSION

Dislocation Dissociation

TEM evidence

A prominent feature of the defect structure of the HT-1 foils is a ribbon-like contrast. Parallel ribbons appear in a single set (I) in Fig. 1 and in four sets (II-V) in Fig. 2a. The ribbons in set V actually contain two segments intersecting at an angle of 10° . The general appearance of the ribbons, together with several other reasons, rules out the possibility of twin bands or precipitates and enables us to identify the ribbons as slip traces. One other reason is that in no case have we observed fringes corresponding to twins or precipitates in place of the ribbons. Nor are extra spots, satellites, or streaks detected in the pertinent selected-area diffraction patterns. Still another reason is that, because the liquid nitrogen trap was not used to cool these two foils during examination, the electron beam exerted a heating effect, which not only produced many ribbons, but also caused some of the pre-existing ribbons to move rapidly in either direction, leading to their extension or contraction (and eventual disappearance). An example of ribbon contraction is seen in the area marked a between Figs. 1a and 1b. Meanwhile, the ribbon marked b in Fig. 1a disappeared in Fig. 1b. The observed reversible motion of the ribbons not just confirms the ribbons being slip traces, it also suggests

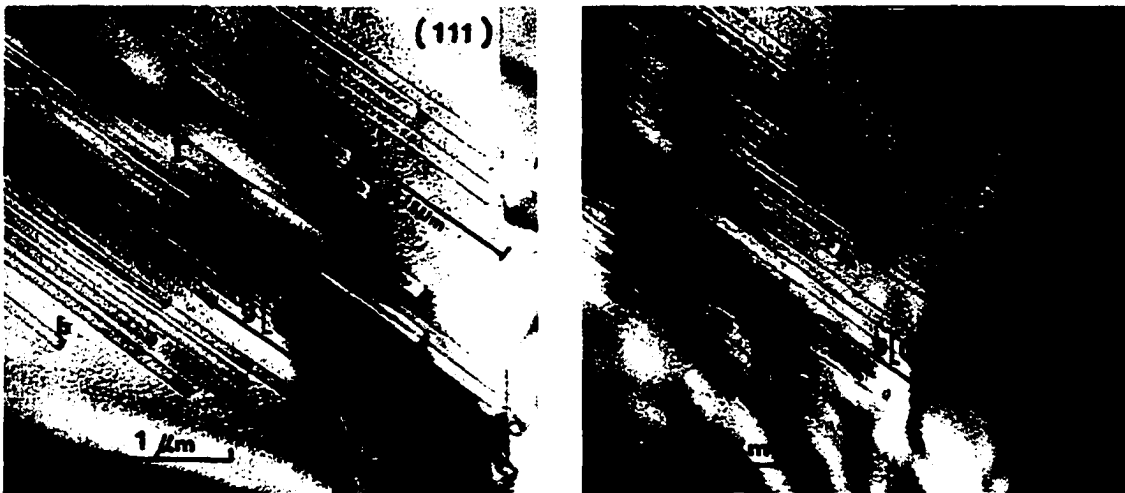
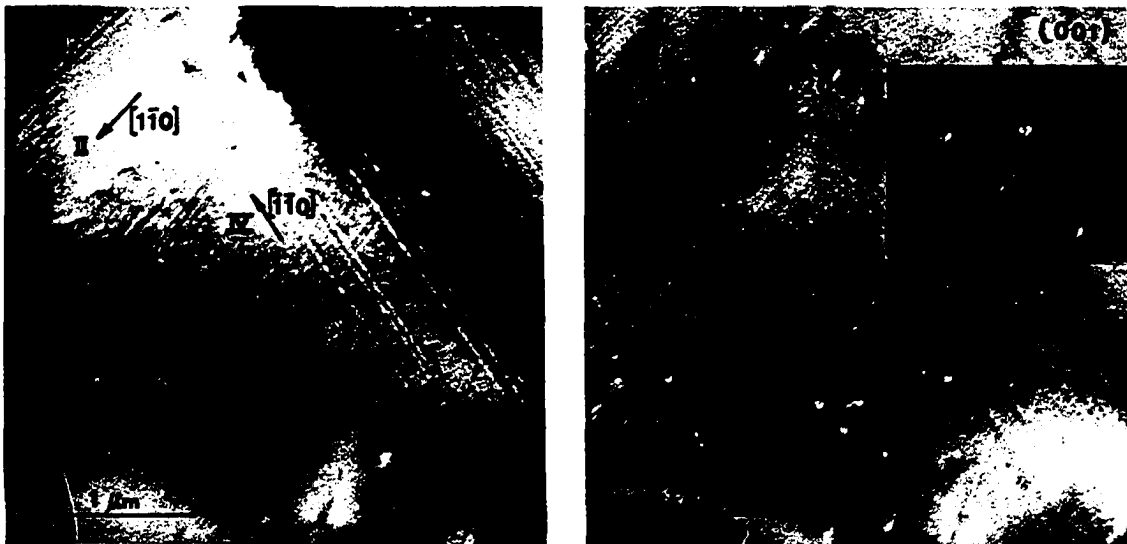


Fig. 1. Electron micrographs taken from the same field of view at ~ 20 sec interval, showing ribbon-like contrast and intermittent movements of some (e.g., a and b) ribbons



(a)

(b)

Fig. 2. Similar ribbon-like contrast observed in another foil of HT-1 Nb. (a) Bright field micrograph. (b) Weak-beam dark-field micrograph revealing fringes at the ribbon heads. Inset gives an enlarged view of four sets of fringes

that the involved dislocations are mainly of the screw character insofar as edge dislocations create slip markings upon leaving the foil.

To ascertain the geometry of the traces and their associated dislocations, the five sets of ribbons in Figs. 1 and 2 and a prominent set of traces in Fig. 3a are analyzed by the stereographic projection method. The latter micrograph was obtained from a third foil of HT-1 Nb with the cold trap in use. None of the traces in Fig. 3a was produced during examination and displayed any mobility. The results of the analyses are summarized in Table 3. Data given in the last three columns disclose the unequivocal choices of the operating slip plane and dislocations for five of the six (except III) sets of traces analyzed. Indeed, the involved dislocations in these five sets are of the screw type, as has been reasoned. Three interpretations are possible for the traces in set III, of which the slip system $(123)[\bar{1}\bar{1}1]$ also implies screw dislocations. However, the large angular deviation (13°) of the ribbon direction from that predicted from the (123) slip plane makes the latter choice somewhat uncertain.

The most important observation in the present work is doubtless the emergence of a double image at almost every front end or head of the slip trace seen in Figs. 1-3. The double image is especially visible in Fig. 3a, for which it should be noted that as the microscopy condition approaches a good two-beam approximation, the double image appears more

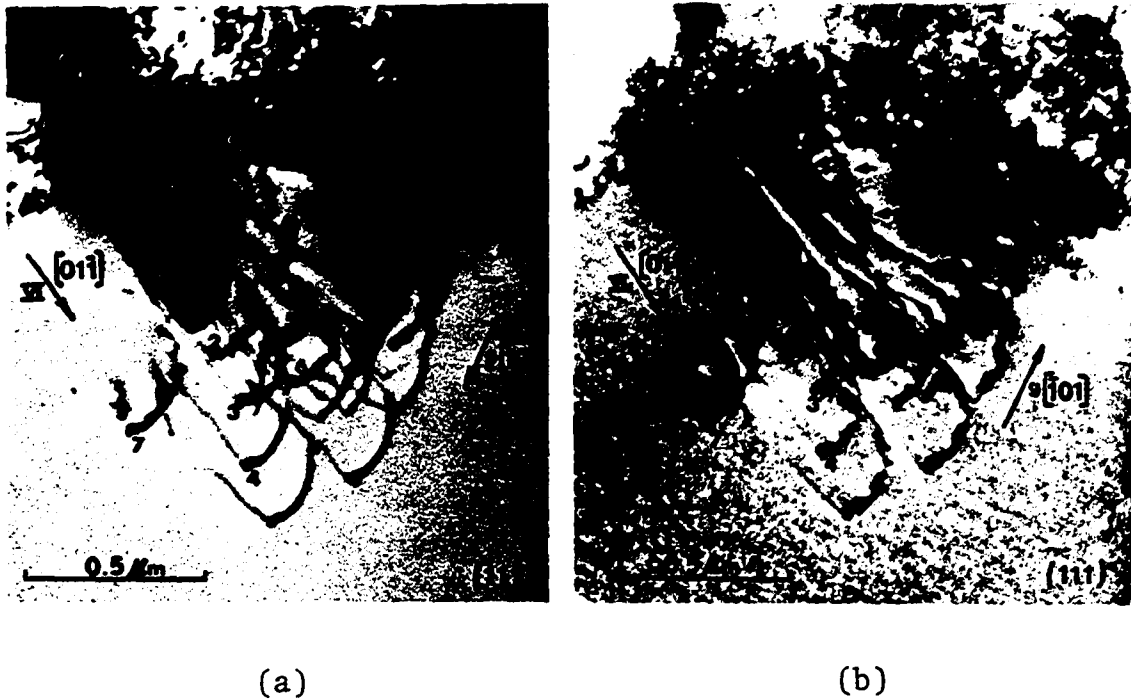


Fig. 3. Diffraction contrast obtained from a third foil of HT-1 Nb. (a) Bright-field micrograph showing double images at the heads of slip traces. (b) Weak-beam dark-field micrograph showing conspicuous fringes in addition to double images at the trace heads

Table 3. Results of the stereographic analyses on the slip dislocations in Figs. 1-3

Fig.	Approx. foil-surface plane	\underline{g} vector	Ribbon set	Nearest direction of ribbons	Possible slip plane	Possible b (screw or edge)
1	(111)	$[0\bar{1}1]$	I	4° off $[0\bar{1}1]$	(211)	$(a/2)[\bar{1}11]$ (S)
2a	(001)	$[\bar{2}00]$	II	6° off $[1\bar{1}0]$	(112)	$(a/2)[\bar{1}\bar{1}1]$ (S)
2a	(001)	$[\bar{2}00]$	III	(i) 13° off $[2\bar{1}0]$	(123) or (121)	$(a/2)[\bar{1}\bar{1}1]$ (S) or $(a/2)[1\bar{1}1]$ (E)
				(ii) 5° off $[3\bar{1}0]$	(132)	$(a/2)[1\bar{1}1]$ (E)
2a	(001)	$[\bar{2}00]$	IV	4° off $[\bar{1}\bar{1}0]$	$(\bar{1}12)$	$(a/2)[1\bar{1}1]$ (S)
2a	(001)	$[\bar{2}00]$	V	7° off $[1\bar{1}0]$	(112)	$(a/2)[\bar{1}\bar{1}1]$ (S)
3a	(111)	$[10\bar{1}]$	VI	6° off $[01\bar{1}]$	(211)	$(a/2)[\bar{1}11]$ (S)

resolved. Moreover, the double images in Fig. 3a exhibit considerable difference between intensities of the two lines in each pair; the front line is always lighter than the back line. Also, some fringes are vaguely seen between the paired lines (e.g., 1 and 2). At this point, we applied the weak beam technique using the $[\bar{1}01]$ reflection and prepared a dark-field micrograph (Fig. 3b). Now all seven trace heads in set VI and many heads in other unnumbered sets display fringe-type contrast. The fringes are particularly conspicuous at four heads marked by arrows. The average length of the fringes is about 130 \AA . A WBDF micrograph was also produced with $\underline{g} = [200]$ from the same field of view shown in Fig. 2a and reproduced in Fig. 2b. In this second WBDF micrograph, practically all trace heads are converted into groups of predominantly three fringes lying in the $[1\bar{1}0]$ direction.

The physical significance of the present results is best seen from the interpretation for the slip traces in sets I (Fig. 1) and VI (Fig. 3) and from that for the contrast produced at the trace heads in Fig. 3. A diagrammatic illustration of the interpretation is given in Fig. 4. The movement of a screw dislocation with $\underline{b} = (a/2)[\bar{1}11]$ on the (211) slip plane produces a pair of parallel markings on the top and bottom surfaces of the foil in the $[01\bar{1}]$ direction. Further movement of the screw to the right will lengthen the trace. However, if the resolved shear stress on the slip plane is reversed as a result of foil bending due to beam heating, the

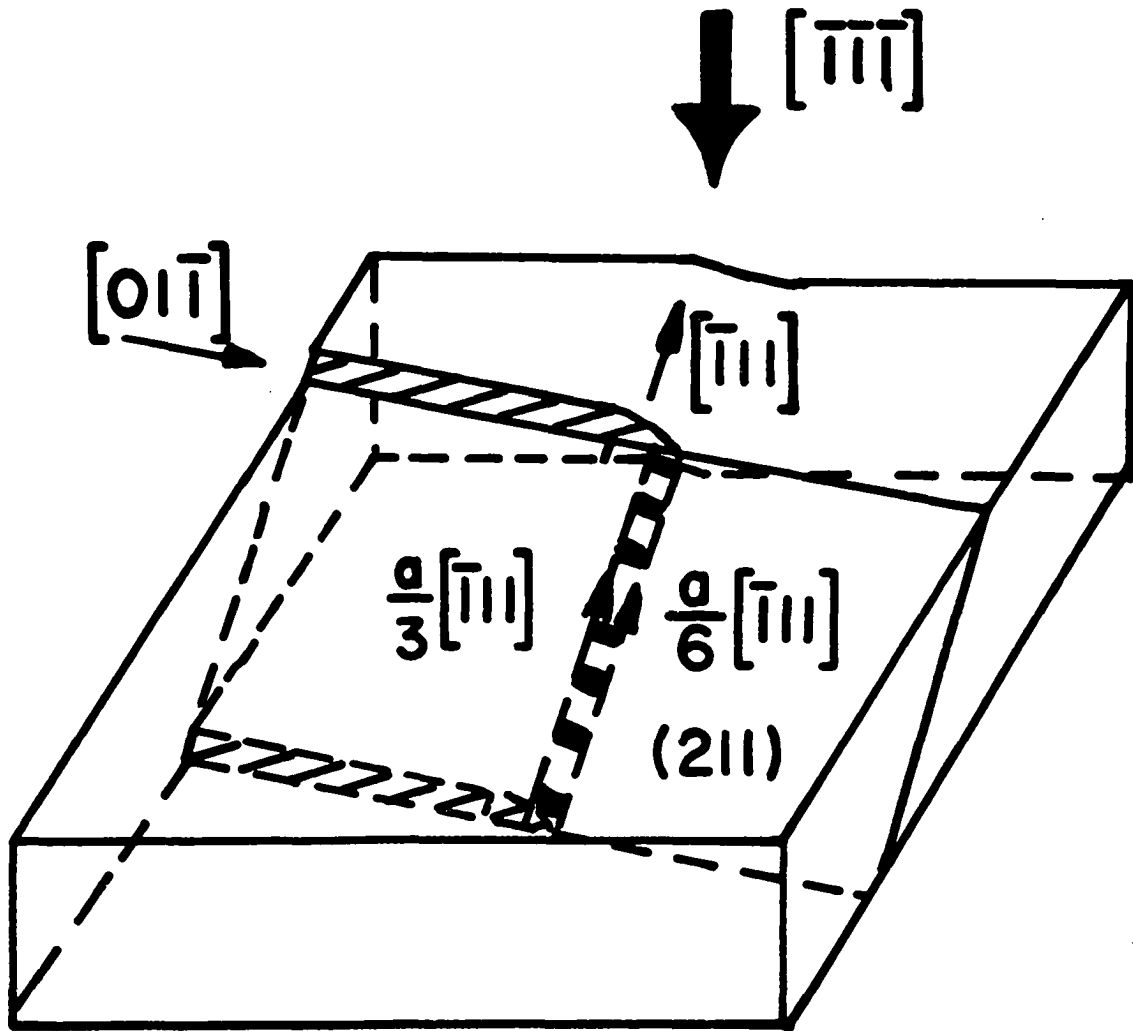


Fig. 4. Diagram illustrating the production of slip markings on the two foil surfaces by the motion of a screw dislocation with $\underline{b} = (a/2)[\bar{1}\bar{1}\bar{1}]$ on the (211) slip plane. The screw at the trace head is shown to split up into two partials with $\underline{b} = (a/6)[\bar{1}\bar{1}\bar{1}]$ in the front and $\underline{b} = (a/3)[\bar{1}\bar{1}\bar{1}]$ in the back

screw will move to left, thus shortening the trace, as is seen at a and b in Fig. 1. We emphasize the movement of screw dislocations here in order to be consistent with (1) the analysis results listed in the table, (2) the frequent observation of cross slip (e.g., trace set V in Fig. 2) in the HT-1 foils, and (3) the contraction of slip traces at a, b, and elsewhere in Fig. 1. All these reasons, especially (3), rule out the participation of edge dislocations in creating slip traces in the present case.

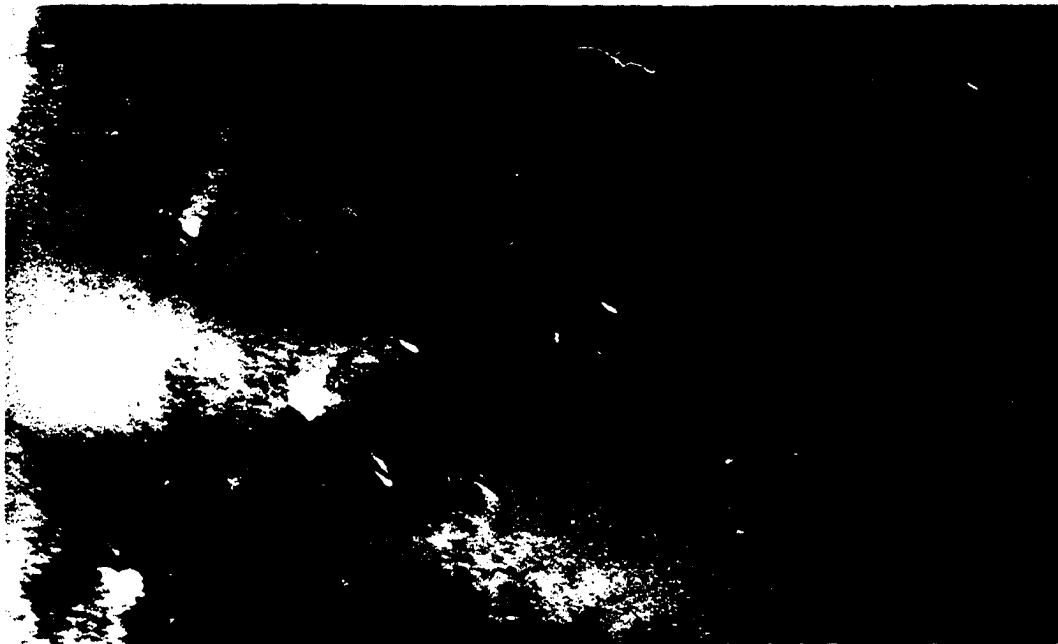
The double images of the trace heads seen in Fig. 3a then imply a dissociation of a perfect screw dislocation into two partials. Hence the fringes revealed by the WBDF technique in Fig. 3b represent the stacking fault enclosed in the extended dislocation. The double image, along with the geometry of the involved slip plane and dislocations and the mobility of the dissociated screws above 20°C, indicates that the dissociation mechanism follows that proposed by Crussard (76), namely,

$$(a/2)[\bar{1}11]_{(211)} \rightarrow (a/3)[\bar{1}11]_{(211)} + (a/6)[\bar{1}11]_{(211)}. \quad (5)$$

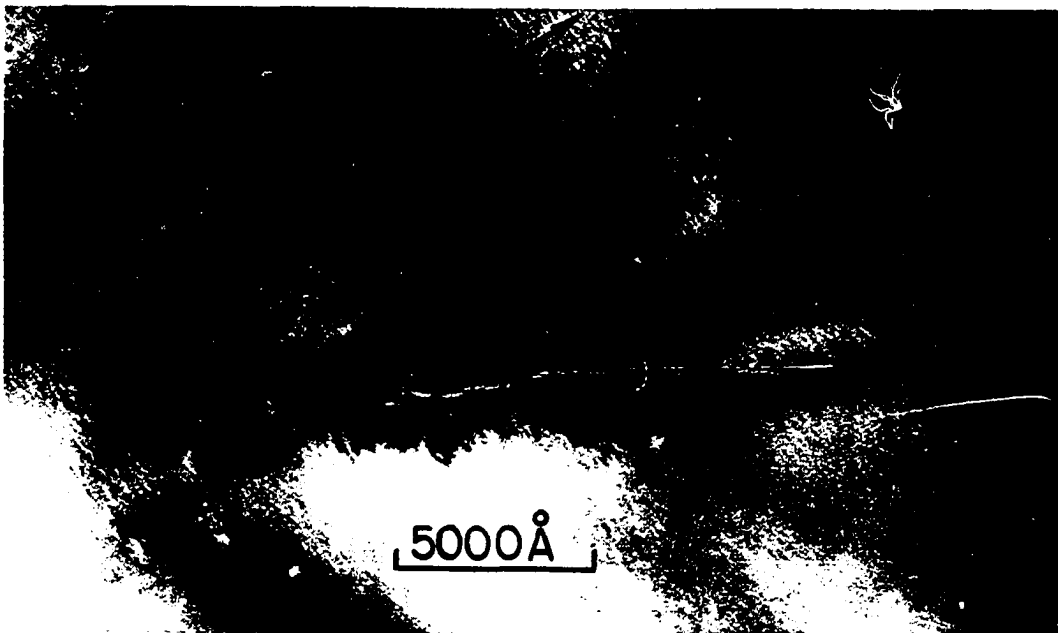
Since the screw splits up into two partials lying on the same plane and since the observed separation between the partials is relatively small, the extended dislocation is capable of moving as the undissociated dislocation. In this mechanism, $|\underline{g} \cdot \underline{b}| = 2/3$ and $1/3$ [for partial dislocations to be visible under $\underline{g} \cdot \underline{b} = 1/3$, see (77)] for the back and front partial dis-

locations, respectively. These values are in accord, at least qualitatively, with the intensity difference observed of the double images in Fig. 3. As far as visibility of the stacking fault is concerned, the displacement vector causing a fault of the type ABCD/CD/EFAB---- in the [211] direction is taken to be $\underline{R} = (1/3)[211]$ (78), which gives $|\underline{g} \cdot \underline{R}| = 1/3$ under the bright- and dark-field conditions in Figs. 3a and 3b. Hence fringes are expected in both micrographs. The fact that only the WBDF micrograph shows sufficiently visible fringes for us to establish the existence of stacking faults at the trace heads is a manifestation of the great advantages of the weak-beam technique in producing defect images of much improved contrast and resolution.

Despite the dissolution of moderate amounts (total 290 wt ppm) of interstitial impurities in the foil matrix of HT-1 foils, screw dislocations were seen to display high mobility ($>2.5 \times 10^{-6}$ cm/sec) at temperature about 30°C. The observed dislocation mobility, coupled with the reversibility of the slip traces, suggests that the present material involves little, if any, segregation of interstitial impurities in the stacking faults. To further confirm that the dissociation was not complicated by interstitial impurities, niobium foils of higher purity have been examined. Foils (Nb-A-1) containing about 100 ppm total interstitial impurities were examined. It is shown in Fig. 5 that dislocations in the front of the slip traces exhibit double images. The bright-field micro-



(a)



(b)

Fig. 5. Nb-A-1 foil which has been tensile strained 2%. (a) Mobile dislocations and their slip traces were revealed in the bright-field (BF) micrograph with $g = [\bar{1}10]$. (b) The images of the partial dislocations were shown by the WADF micrograph with $g = [10\bar{1}]$

graph in 5(a) was taken under a three beam condition with $\underline{g} = \pm [110]$ of equal intensity, and the weak-beam dark micrograph in 5(b) was taken by tilting the foil so as to move the $[101]$ diffraction spot to the center of the diffraction pattern. The Burgers vector of the dislocation is $(a/2)[\bar{1}11]$ before dissociation and the width of the separation between partials is $105 \pm 15 \text{ \AA}$.

The bright-field micrograph shown in Fig. 6 is one of several obtained from HT-8 foils, which contained 90 ppm total interstitial impurities. Again the dislocations yielded double images despite the fact that the micrograph was taken under excellent two beam conditions. The perfect dislocations have the Burgers vector $(a/2)[11\bar{1}]$, which was determined from the clearly observed cross slip directions A and B marked on the micrograph. The dislocations dissociate on the $\{121\}$ planes and the width between the double images is about 120 \AA . Also worth noting is the difference in the intensity of the two images as mentioned previously; the front image is weaker than the rear one in accord with the Crussard Model. There is a possibility, however, that the double images observed in Fig. 6 may be due to the conditions that $\underline{g} \cdot \underline{b} = 2$ and $s_g = 0$ (79).

Mobile dislocations in Irr-1 A-10 foil exhibit the same type of separation under good two beam conditions. A pair of bright- and dark-field micrographs is shown in Fig. 7. The

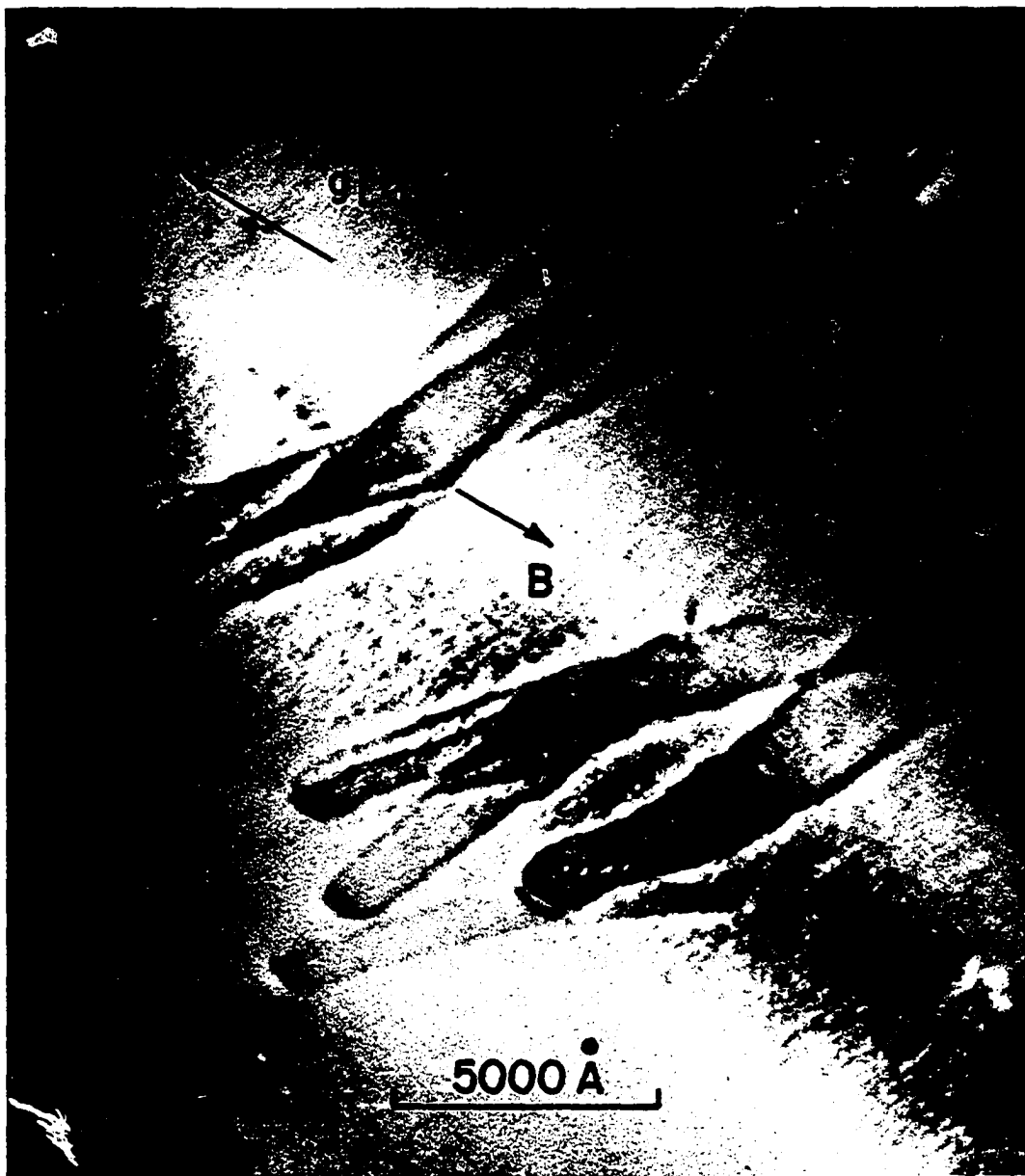


Fig. 6. Double images were observed at the front of the slip traces in the BF micrograph with $g = [\bar{1}\bar{1}2]$. Arrows A and B indicate the cross-slip direction $[\bar{1}11]$

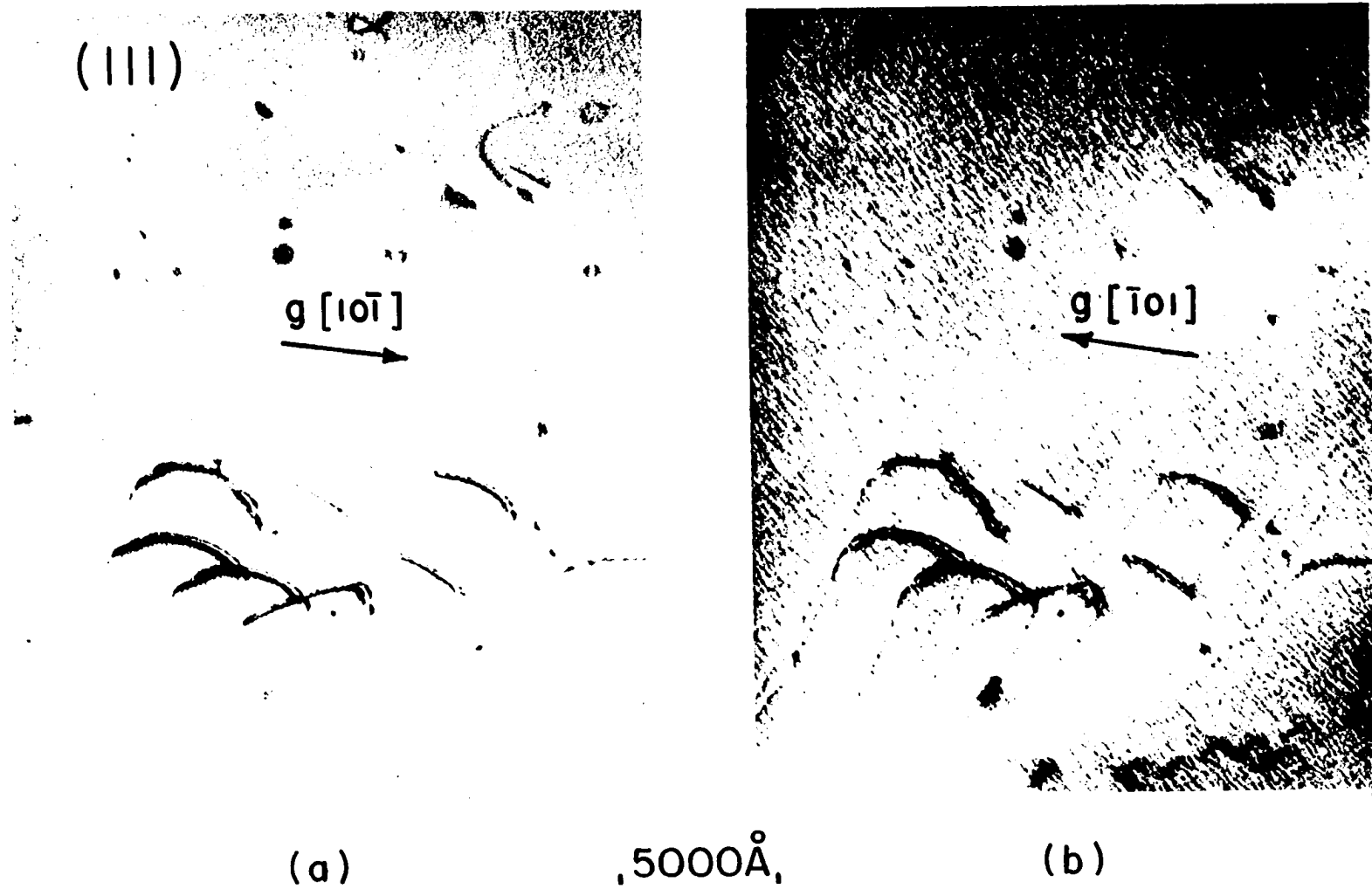


Fig. 7. Nb-Irr-1 foil annealed at 1000°C exhibits a group of dislocations with double images. (a) BF micrograph with $g = [10\bar{1}]$. (b) DF micrograph with $g = [\bar{1}01]$

perfect dislocation has a Burgers vector $(a/2)[11\bar{1}]$, but the slip plane could not be identified. The separation between the paired dislocations seems to vary from one end to the other.

Stacking fault energy

In higher purity A -1 and HT-8 foils, the dissociation and the extended dislocations were observed similar to those in HT-1 foils. To estimate the stacking fault energy γ_{SF} of Nb, the equation derived for anisotropic bcc crystals by Chou (80) from the Crussard mechanism is applied, which is expressed as

$$d = K_s b^2 / 9\pi\gamma_{SF} \quad (6)$$

where K_s is a composite elastic constant. For Nb, $b = 2.86 \text{ \AA}$, and $K_s = 4.429 \times 10^{11} \text{ dyne/cm}^2$ (81). The observed separation of $d \sim 120 \text{ \AA}$ then implies a value of $\gamma_{SF} = 10 \text{ ergs/cm}^2$. This value is of the same order of magnitude as that suggested ($\gamma_{SF} = 21 \text{ ergs/cm}^2$) by Wasilewski (72), otherwise it is too small in comparison with values suggested by other authors (70-72). A recent paper by Welsch et al. (82) on Ta and Ta-N alloys showed that $(a/2)\langle 111 \rangle$ dislocations have a width of about 40 \AA . These authors did not discuss the possibility of a dissociation according to Crussard model. If Equation 6 is used to calculate γ_{SF} from $d = 40 \text{ \AA}$ using other appropriate values for Ta: $K_s = 6.105 \times 10^{11} \text{ ergs/cm}^2$ and $b = 2.85 \text{ \AA}$ (83), γ_{SF} turns out to be 39 ergs/cm^2 for Ta, which is also close

to Wasilewski's value of 41.4 ergs/cm^2 .

An important point should be mentioned here that in no case has the possibility of enhancing the dissociation of dislocations by interstitial impurities been observed in this study. With oxygen content changing from 9 to 199 wt ppm, the width of the separation in Nb remains about the same. Welsch et al. (82) detected a small decrease of the width of dislocation with increasing content of N from 5 to 15000 at. ppm in Ta, however.

Seidman and Burke (84) have recently examined the dislocation dissociation in Mo by FIM. Their results indicate that the separation of partials decrease from 60 \AA to 40 \AA as the resistivity ratio ($R_{300^\circ\text{K}}/R_{4.2^\circ\text{K}}$) of their Mo specimen was decreased from 2200 to 33. Although Welsch et al. (82) suspected that the FIM might give a separation two-three times greater than the value given by TEM, they agreed that an increase in the content of interstitial impurities would not increase the width of screw dislocations. In fact, according to the data shown in Fig. 8, the width of dislocations should decrease as the total interstitial impurity contents are increased.

The information thus far quoted seems to suggest that interstitial impurities in cluster form tend to hinder the separation of partial dislocations instead of enhancing the dislocation dissociation by forming the Suzuki atmosphere in

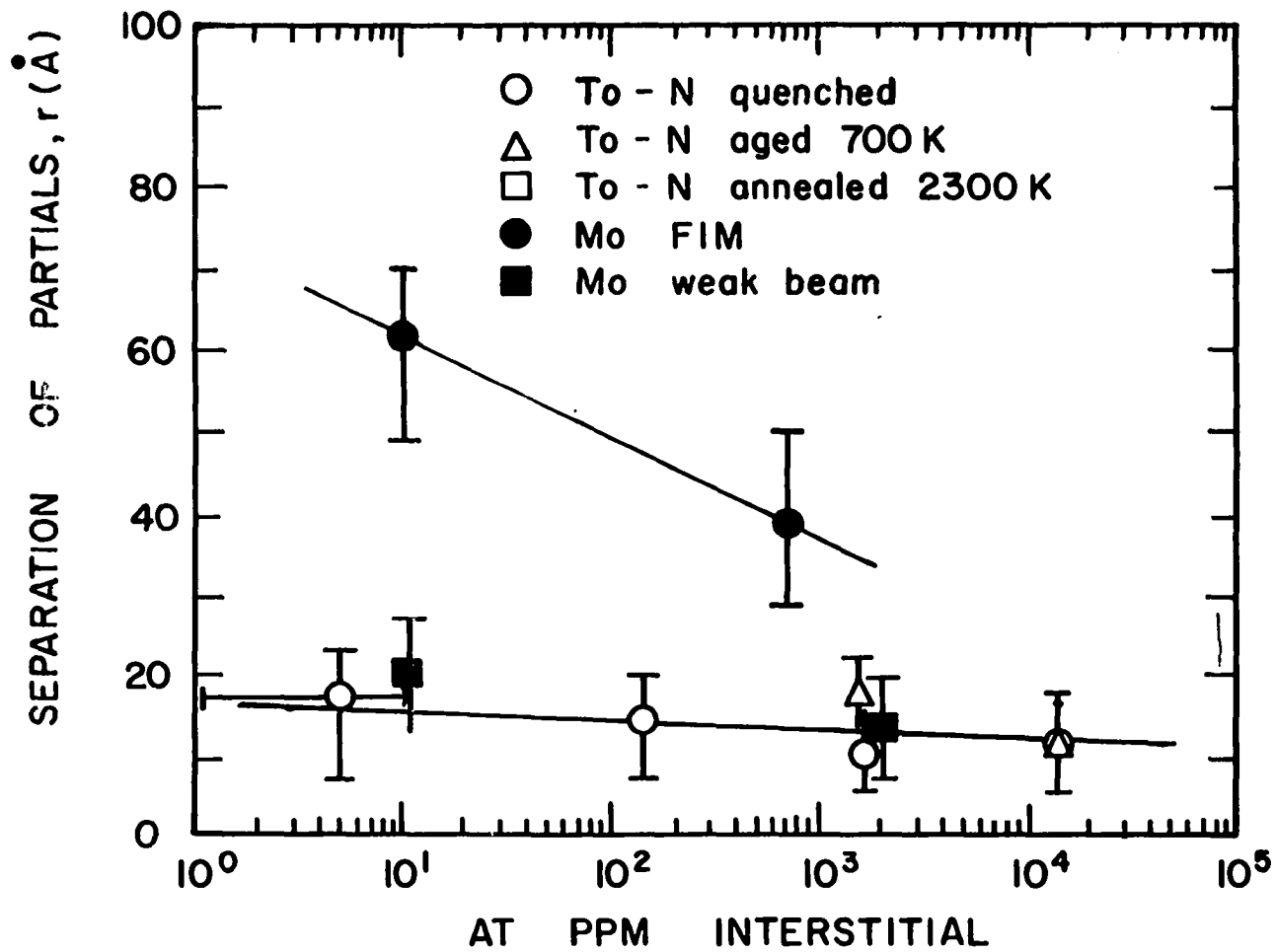


Fig. 8. Results reported by Welsch *et al.* (82) showing the effect of interstitial impurity content on the width of screw dislocations in Ta and Mo evaluated by FIM and WBDF techniques

the faulted regions.

Dislocation Interactions

Interactions between two glissile dislocations

An observation obtained from HT-1 is shown in Fig. 9. Six slip bands are seen along the $[01\bar{1}]$ direction in the (011) planes produced by glissile dislocations with $\underline{b} = (a/2)[1\bar{1}1]$. While five (1 to 5) such dislocations appeared as single wavy lines, the sixth consists of two segments, Aa and Bb, in an intricate pattern. To elucidate the diffraction contrast in the encircled region, we first note that both segments are attached to another dislocation CD at a and b. Based on the information derived from Fig. 9 and the associated electron diffraction pattern (EDP, not shown), it is reasonable to assume the latter dislocation to be a glissile dislocation also, with $\underline{b} = (a/2)[\bar{1}11]$ in the (110) plane. Since CD generated no slip traces, this dislocation must have been immobile, and could act as an obstacle to moving dislocations. A plausible interpretation of the contrast in the encircled region is depicted in Fig. 10. Diagram 10(a) shows an $(a/2)[1\bar{1}1]$ glissile dislocation CD in the (110) plane. Apparently, the former dislocation was moving at a relatively low speed; otherwise it would have cut through the immobile dislocation. On the other hand, from the entanglement seen in Fig. 9, A_1B_1 must have been attracted elastically to CD. An interaction is thus envisaged between A_1B_1 and CD around



Fig. 9. Dislocations appeared at the front of slip traces 1-6 in Nb-HT-1 foil

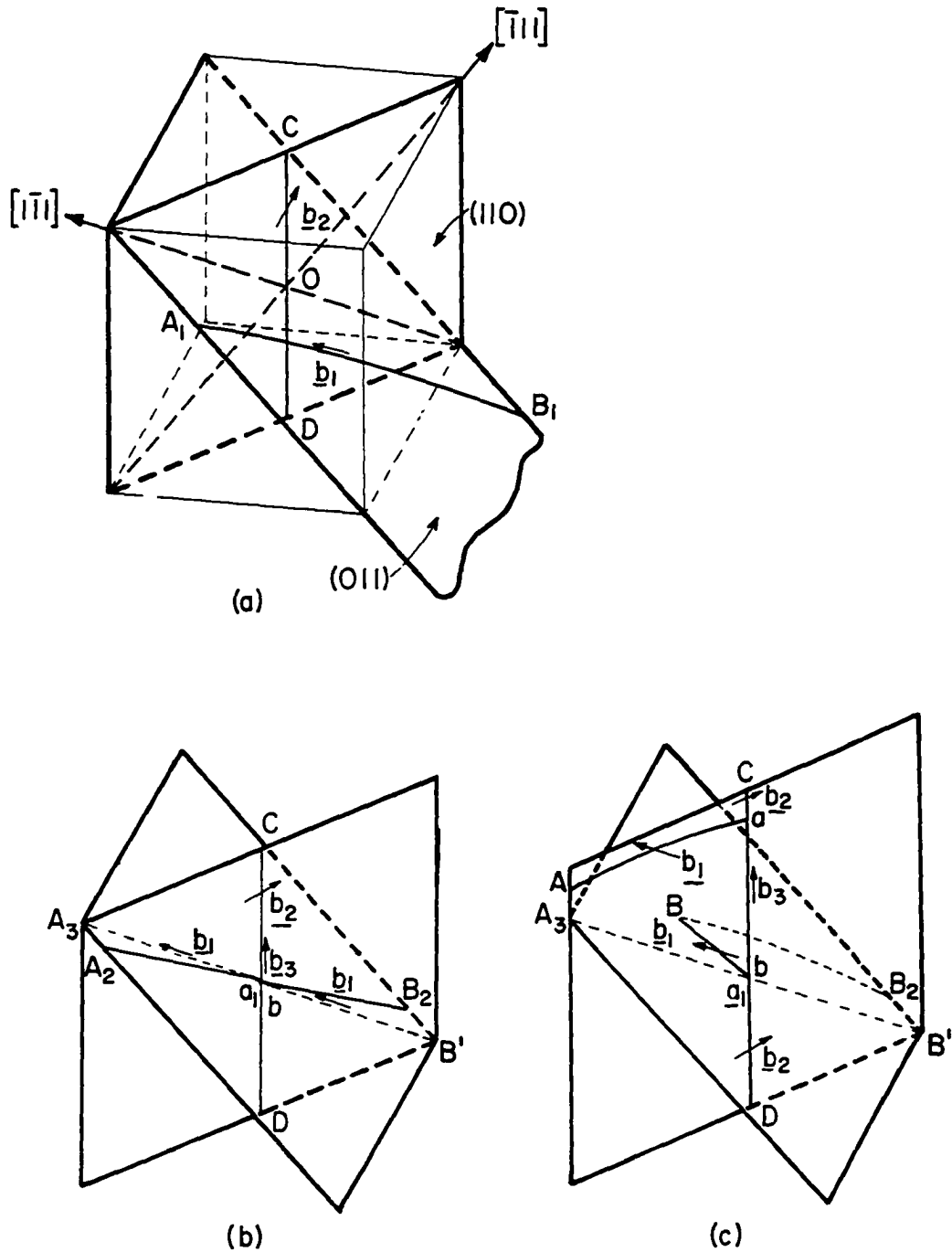
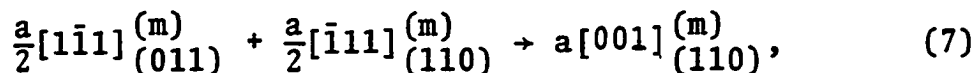


Fig. 10. Diagrams illustrating the interpretation of the dislocation morphology observed in the encircled region in Fig. 8. (a) Before and (b) after Reaction 7; (c) further reaction expressed by 8 between A_3a_1 and Cd and the operation of bB_2 as a Frank-Read mechanism lead to the final distribution of dislocations

the contact point 0 as follows:

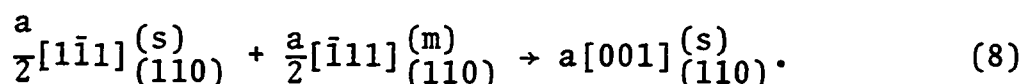


where the superscripts indicate the character of the dislocations, being pure edge (e), pure screw (s) or mixed (m). Although the product dislocation lies in a slip plane, its $a[001]$ Burgers vector disqualified it as a glissile. Also, since Reaction 7 must proceed along the line of intersection between the reactant-dislocation planes, the product sessile dislocation a_1b must originally lie in the $[1\bar{1}1]$ direction, as shown in Fig. 10(b). The interaction 7 would not only momentarily halt the motion of A_2B_2 , but also split A_2B_2 into two segments, A_2a_1 and bB_2 , connected by a sessile a_1b . To reconcile between Fig. 10(b) and Fig. 9, we assume that at the time of interaction, B_2b has already passed the intersection line A_3B' between (011) and (110), thus making it impossible for segment B_2b to cross-slip.¹ But this segment could act as either a Frank-Read source or a Frank-Read mechanism (85), depending on whether or not the segment is pinned on the foil surface at B_2 . The shape of the image line bBB_2 in Fig. 9 suggests that bB_2 has acted as a Frank-Read mechanism,

¹Even if the position of B_2b was at or behind the intersection line A_3B' at the time of interaction, cross slip could not have occurred as did A_2a_1 . The reason is simply geometric because if reaction 7 proceeds upward along ba for A_2a_1 , the same reaction must proceed downward along bD for B_2b , which is against the resolved shear stress, thus disallowed.

whose operation enabled bB_2 to swing around the pinning point b to Bb . In so doing, the slip trace was extended from B_2 to B and the dislocation segment reached a stable configuration, wherein zero net line tension is acting on the segment.

The other segment A_2a_1 , meanwhile, would first advance to the intersection position A_3a_1 . At this position, it had the options to either act as a Frank-Read mechanism (or source) or cross slip. Apparently the latter option was exercised, which enabled A_3a_1 to switch the slip plane from (011) to (110) and the slip process to continue in a "restricted" manner. By "restricted" is means that the cross slip is accompanied by an interaction between A_3a_1 and CD similar to reaction 7, except that the $(a/2)[\bar{1}\bar{1}1]$ dislocation, too, lies in the (110) plane. Hence the correct expression is



Another feature of reaction 8 is the line direction of the product dislocation, which can be any within the (110) plane. In the present case, however, because CD is immobile, reaction 8 simply converts CD into a sessile along the original line. In other words, after reaction 8, segment ab becomes a sessile with $\underline{b} = a[001]$, whereas the rest of CD is still a glissile with $\underline{b} = (a/2)[\bar{1}\bar{1}1]$. The occurrence of reaction 8 is nontrivial because the separation between a and b exceeds 2000 \AA . Such a large separation rules out the possibility of a pole mechanism which may operate in other cases to effect

the split of AB into two segments. The plane difference between 8 and 7 qualifies ab to be a pure screw sessile, whereas a_1b has a mixed character.

The dislocation morphology seen in Fig. 9 is by no means accidental. Neither is it confined to one specimen, nor to one grade of Nb. To indicate the recurrence of such morphology, another micrograph taken from HT-8 is shown in Fig. 4.. Attention is again directed to the encircled region. Using the same notation, it is seen that the latter micrograph also features a slip band marked 1, at the front of which exist two segments, Aa and bB, attached to another dislocation. Note the striking resemblance between the encircled regions in Figs. 9 and 11. Experimental difficulties with HT-8, however, prevented us from getting adequate data for a precise interpretation of Fig. 11.

Interactions between dislocation loops and dislocations in a group

Fig. 12 shows the diffraction contrast of a number of dislocations in HT-2, which has the lowest purity. The prominent dislocations in this figure include (1) a group of dislocations whose images appear as faint, approximately parallel lines, (2) one large loop in the upper left corner, and (3) one smaller loop in the lower right corner. An interesting feature of this micrograph is the step-wise or zigzag appearance of the two loops on one side and the "barely" broken

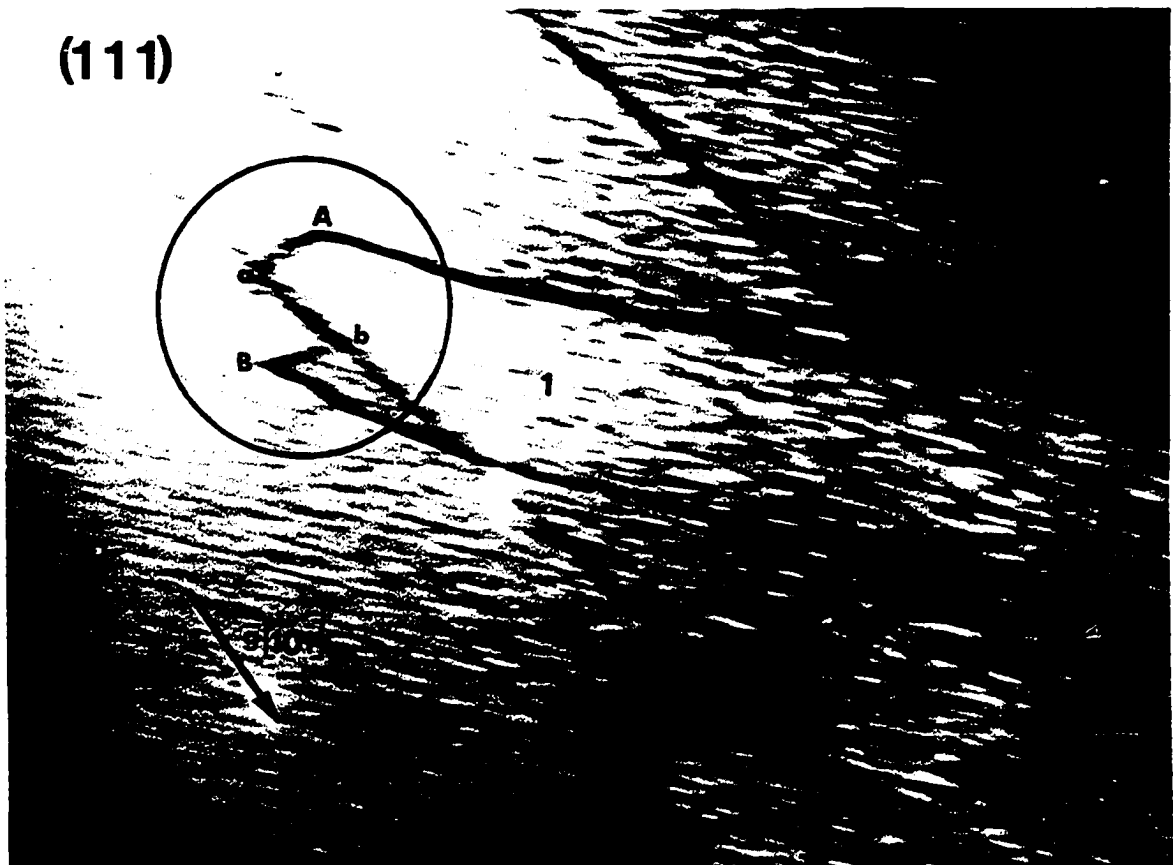


Fig. 11. A similar distribution of dislocations observed in Nb-HT-8. Note the striking resemblance in dislocation morphology between the encircled regions in Figs. 9 and 11

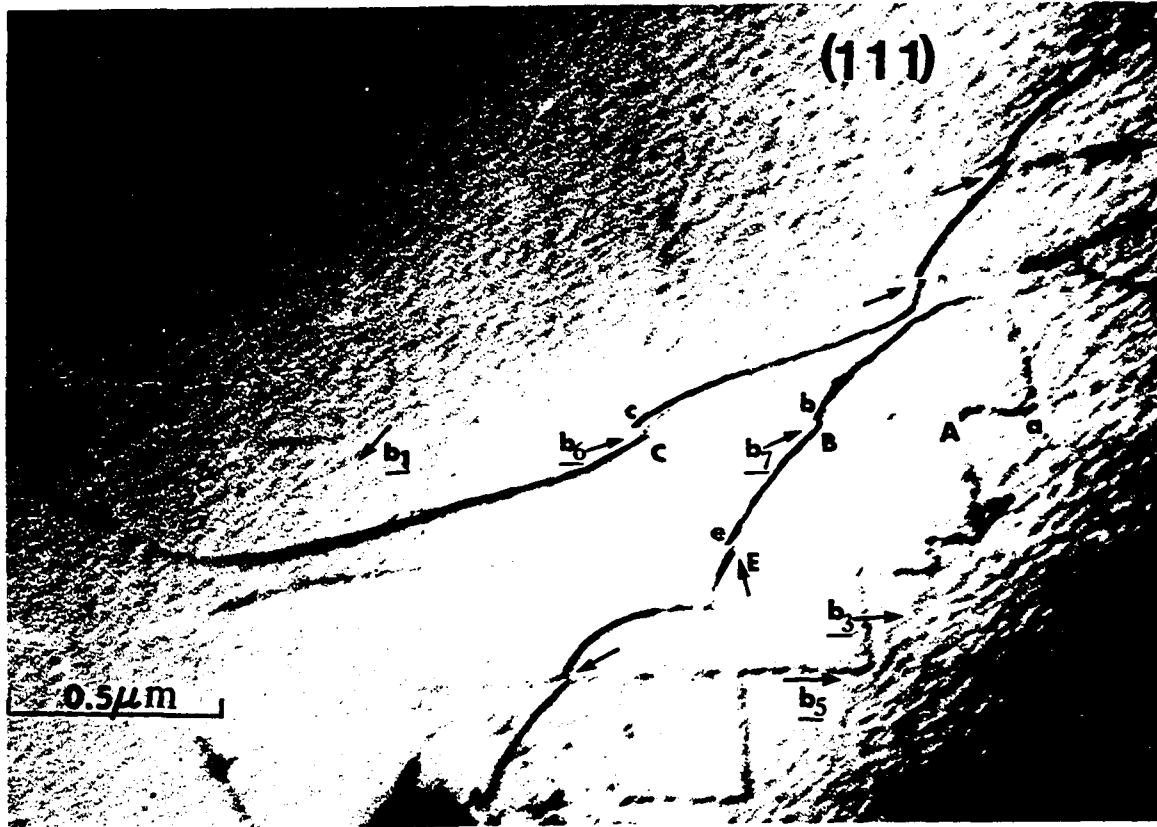


Fig. 12. Nb-HT-2 displayed a group of approximately parallel dislocations with b_1 and two loops with b_2 and b_3 under $g_1 = [\bar{1}01]$

appearance on the other side. At this point, it is important to prove that the discontinuities marked by arrows along one side of the loops are not caused by the well-known TEM phenomenon that the contrast of a dislocation changes side with respect to the line position of the dislocation with or without breakage when $(\underline{g} \cdot \underline{b})_s$ reverses its sign for $n(\equiv \underline{g} \cdot \underline{b}) = 2$ or 1 where s is the deviation parameter. The proof was established in a second micrograph taken from the same field of view under $\underline{g} = [\bar{1}2\bar{1}]$ shown in Fig. 13. Because of a large tilting of the foil, the latter micrograph displays uniformly low contrast. Despite the poor quality, it serves to disclose relatively strong contrast at the discontinuities C_c and E_e in comparison with the connecting dislocations. Overexposures of Fig. 13 reveal similar, though weaker, contrast at other discontinuities marked by arrows. Also of importance is the fact that the contrast at C_c and E_e shows finite lengths of ~ 400 and $\sim 150 \text{ \AA}$, respectively. These results thus rule out the possibility that the "barely" broken appearance on one side of the two loops is due to the TEM effect caused by a change in sign of the quantity $(\underline{g} \cdot \underline{b})_s$.

Fig. 12 clearly shows that the Group (1) dislocations have interacted with the two loops in different modes on opposite sides, leading to the formation of steps on one side and "bare" discontinuities on the other. To attempt an interpretation of this dislocation morphology, we quickly came to



Fig. 13. Strong contrast of finite lengths at Cc and Ee under $g_2 = [\bar{1}2\bar{1}]$ rules out the possibility that the discontinuities, Bb, Cc and Ee, are caused by the diffraction effect as a result of change in sign of the quantity $(\underline{g}\cdot\underline{b})_s$. Magnification same as in Fig. 12.

realize that even the simplest interaction, namely $\underline{b}_1 + \underline{b}_2 \rightarrow \underline{b}_3$, would necessitate four to seven Burgers vectors. The number of Burgers vectors that we must deal with readily reveals the impracticality of applying the $\underline{b} \parallel \underline{g}_1 \times \underline{g}_2$ method for the determination of the \underline{b} 's as well as the impossibility of attaining complete information. Under these circumstances, we are forced to attempt an interpretation by deduction and elimination of less satisfactory alternatives. Despite the obvious difficulties, the interpretation offered below is consistent with the main TEM results shown in Figs. 12 and 13 and with the EDP data.

The interpretation is based largely on the visibility or invisibility of various dislocations under two \underline{g} vectors, $[\bar{1}01]$ and $[\bar{1}2\bar{1}]$, together with their line direction summarized in Table 4. The visibility of the Group (1) dislocations under $\underline{g}_1 = [\bar{1}01]$ is assumed to be of the "near invisibility" category (43) in the sense that $\underline{g}_1 \cdot \underline{b}_1 = 0$, thus invisible for the screw components; but $(1/8)(\underline{g}_1 \cdot \underline{b}_1 \times \underline{v}_1) > 0.08$, thus visible for the edge components. The Burgers vectors of the three interacting dislocations are denoted \underline{b}_1 , \underline{b}_2 , and \underline{b}_3 in the same sequence as previously cited. From our experience gained in the extensive study of dislocation dissociation, we assume that these dislocations are perfect glissiles in the $\{011\}\langle 1\bar{1}1 \rangle$ slip systems. In applying the simple equation of interaction, use is made of the property,

Table 4. Visibility and line directions of dislocations in Figs. 11 and 12

	The Burgers Vector						
	\underline{b}_1	\underline{b}_2	\underline{b}_3	\underline{b}_4	\underline{b}_5	\underline{b}_6	\underline{b}_7
Visibility under $\underline{g}_1 = [\bar{1}01]$	--- ^a	yes	yes	yes	yes	no	no
Visibility under $\underline{g}_2 = [\bar{1}2\bar{1}]$	weak	weak	weak	weak	weak	yes	yes
Line direct on, \underline{v}	$[11\bar{1}]$	loop	loop	$[1\bar{1}1]$	$[11\bar{1}]$	--- ^b	--- ^b

^aNearly invisible. See text for explanation.

^bSegments are too short for an accurate determination of their line directions.

$\underline{b}_m \times \underline{v}_m = \pm \underline{n}$ for two segments of a loop on the opposite sides, where \underline{n} is the unit vector in the direction normal to the plane of the loop (86). When the same line vector \underline{v}_m is used, this property is equivalent to representing the two segments by the same Burgers vector with opposite signs; that is, by $\pm \underline{b}_m$. Consequently each loop generates two interactions of the form $\underline{b}_1 \pm \underline{b}_2$ (or \underline{b}_3) \rightarrow \underline{b}_4 and \underline{b}_6 (or \underline{b}_5 and \underline{b}_7) on the two sides of the loop.

The visibility conditions listed in Table 4 greatly limit the selection of the first three Burgers vectors. For instance, for the two loops to be visible under $\underline{g}_1 = [\bar{1}01]$, the $\underline{g} \cdot \underline{b} \neq 0$ condition would confine \underline{b}_2 and \underline{b}_3 to $\pm (a/2)[11\bar{1}]$ or $\pm (a/2)[\bar{1}11]$. Also, for the line dislocations to be invisible under $\underline{g}_1 \cdot \underline{b}_1 = 0$, \underline{b}_1 must be either $\pm (a/2)[111]$ or $\pm (a/2)[\bar{1}\bar{1}1]$. Combining these possible \underline{b} 's yields four alternative sets of interactions, none of which offers a completely satisfactory interpretation. By comparison, however, the following set of interactions has the least inconsistency in explaining the observations.

Large loop on its left-hand side: $(\underline{g}_1 + \underline{b}_2 \rightarrow \underline{b}_4)$

$$\frac{a}{2}[1\bar{1}1]_{(011)}^{(m)}[\bar{1}1\bar{1}] + \frac{a}{2}[\bar{1}11]_{(110)}^{(m)}[100] \rightarrow a[001]_{(110)}^{(m)}[\bar{1}\bar{1}1], \quad (7-1)$$

Large loop on its right-hand side: $[\underline{b}_1 + (-\underline{b}_2) \rightarrow \underline{b}_6]$

$$\frac{a}{2}[1\bar{1}1]_{(011)}^{(m)}[\bar{1}1\bar{1}] + \frac{a}{2}[\bar{1}\bar{1}\bar{1}]_{(110)}^{(m)}[100] \rightarrow a[1\bar{1}0], \quad (9-1)$$

Smaller loop on its right-hand side: $(\underline{b}_1 + \underline{b}_3 \rightarrow \underline{b}_5)$

$$\frac{a}{2} [1\bar{1}\bar{1}]_{(011)}^{(m)} [11\bar{1}] + \frac{a}{2} [\bar{1}\bar{1}\bar{1}]_{(101)}^{(m)} [\text{loop}] \rightarrow a [001]_{(\bar{1}\bar{1}0)}^{(m)} [11\bar{1}], \quad (7-2)$$

Smaller loop on its left-hand side: $[\underline{b}_1 + (-\underline{b}_3) \rightarrow \underline{b}_7]$

$$\frac{a}{2} [1\bar{1}\bar{1}]_{(011)}^{(m)} [11\bar{1}] + \frac{a}{2} [\bar{1}\bar{1}\bar{1}]_{(101)}^{(m)} [\text{loop}] \rightarrow a [1\bar{1}0]. \quad (9-2)$$

Note that the Burgers vectors of the product dislocations on the equivalent side of the two loops are identical. This coincidence reduces the total number of Burgers vectors involved from seven to four. To substantiate these interactions, Table 5 lists the calculated values of $\underline{g}_i \cdot \underline{b}_m$ and $(1/8)(\underline{g}_i \cdot \underline{b}_m \times \underline{v}_m)$. As shown by the check marks in parentheses, the calculated results agree with the observed visibilities or invisibility in Figs. 12 and 13 in all respects except the dot products of \underline{b}_6 and \underline{b}_7 with \underline{g}_1 . These disagreements are considered relatively less serious because they are connected with the dislocations of extremely short lengths, from which the diffraction contrast is difficult to establish.

By virtue of these four interactions, we are now in a position to describe what might have happened in Fig. 12. Fig. 14(a) shows that the large and smaller loops probably preexisted with smooth lines in the (110) and (101) planes, respectively. Then a group of nearly parallel glissile dislocations were activated to move on different (011) planes toward the loops. Each time a dislocation in the Group

Table 5. Verification of Reactions (7-1), (7-2), (9-1) and (9-2) adopted to interpret the dislocation morphology observed in Figs. 11 and 12. Check marks and crosses in parentheses indicate the agreement and disagreement, respectively, between the calculated values of $\underline{g}_i \cdot \underline{b}_m$ or $(1/8)(\underline{g}_i \cdot \underline{b}_m \times \underline{v}_m)$ and the observed diffraction contrast

Part A. Reactions (7-1) and (9-1) of the Group (1) dislocations with the large loop

\underline{b}_m	$\underline{b}_1 = \frac{a}{2}[1\bar{1}1]$	$\underline{b}_2 = \pm \frac{a}{2}[\bar{1}11]$	$\underline{b}_4 = a[001]$	$\underline{b}_6 = a[1\bar{1}0]$
$\underline{g}_1 \cdot \underline{b}_m$	0 (✓)	$\pm 1^a$ (✓)	1 (✓)	-1 (X)
$\underline{g}_2 \cdot \underline{b}_m$	-2 (✓)	$\pm 1^a$ (✓)	-1 (✓)	-3 (✓)
$\underline{b}_m \times \underline{v}_m$	[011]		[110]	
$\frac{1}{8}(\underline{g}_1 \cdot \underline{b}_m \times \underline{v}_m)$	0.125 (✓)		-0.125 (✓)	Criterion inapplicable
$\frac{1}{8}(\underline{g}_2 \cdot \underline{b}_m \times \underline{v}_m)$	0.125 (✓)		+0.125 (✓)	

^aFor pure screw segments only.

Table 5. (Continued)

Part B. Reactions (7-2) and (9-2) of the Group (1) dislocations with the smaller loop				
\underline{b}_m	$\underline{b}_2 = \frac{a}{2} [1\bar{1}1]$	$\underline{b}_3 = \pm \frac{a}{2} [\bar{1}11]$	$\underline{b}_5 = a [001]$	$\underline{b}_7 = a [1\bar{1}0]$
$\underline{g}_1 \cdot \underline{b}_m$	0 (✓)	$\pm 1^a$ (✓)	1 (✓)	-1 (X)
$\underline{g}_2 \cdot \underline{b}_m$	-2 (✓)	$\pm 1^a$ (✓)	-1 (✓)	-3 (✓)
$\underline{b}_m \times \underline{v}_m$	[011]		$[\bar{1}10]$	
$\frac{1}{8} (\underline{g}_1 \cdot \underline{b}_m \times \underline{v}_m)$	0.125 (✓)		0.125 (✓)	Criterion inapplicable
$\frac{1}{8} (\underline{g}_2 \cdot \underline{b}_m \times \underline{v}_m)$	0.125 (✓)		0.375 (✓)	

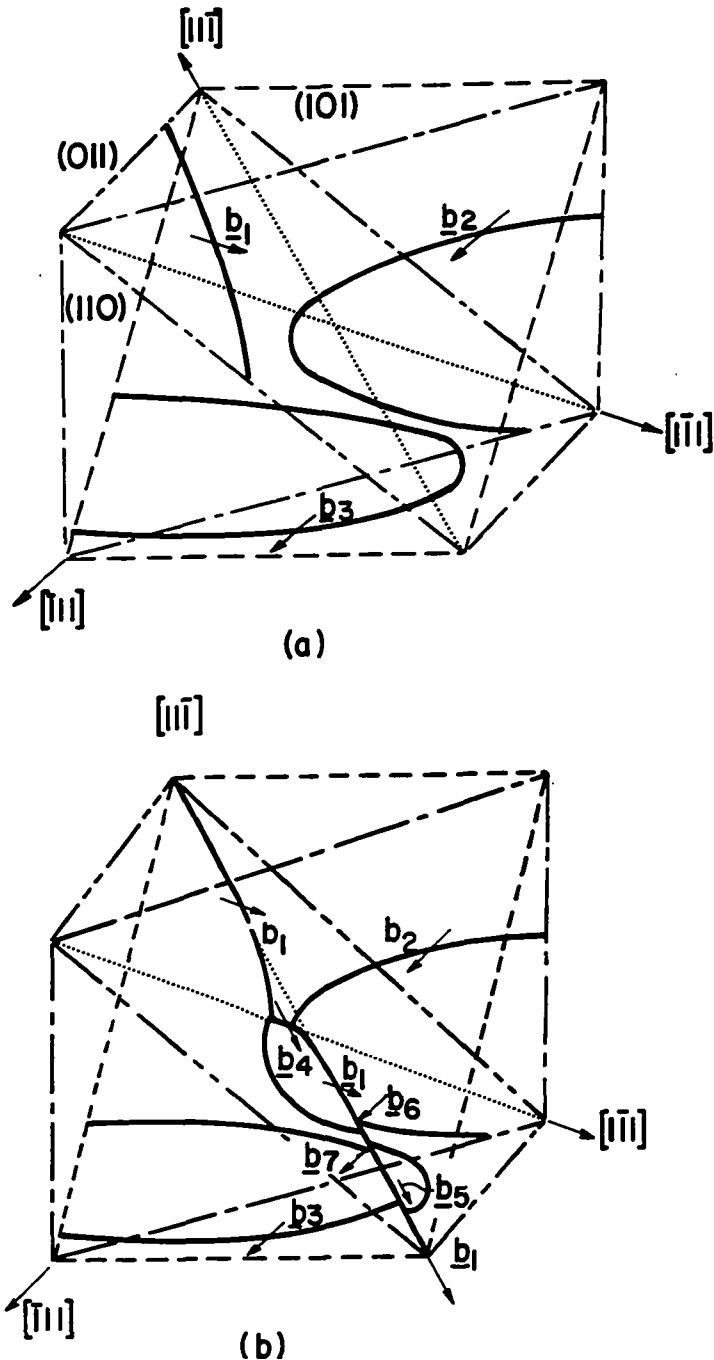


Fig. 14. A possible interpretation of the dislocation morphology observed in Fig. 12. (a) A large loop with \underline{b}_2 and a smaller loop with \underline{b}_3 preexist in the (110) and (101) planes, respectively. An activated dislocation with \underline{b}_1 is moving in the (011) plane toward the loops. (b) The interactions, 7 and 9, between the moving dislocation and the loops create a step with \underline{b}_4 (or \underline{b}_5) = $a\langle 001 \rangle$ and a discontinuity with \underline{b}_6 (or \underline{b}_7) = $a\langle 110 \rangle$ on the opposite side of the loops

approached a loop, interactions 7 and 9 took place concurrently on opposite sides as shown in Fig. 14(b). A direct result of these interactions is the conversion of the segments Aa, Bb, Cc, and Dd from glissile to sessile with $\underline{b} = a\langle 001 \rangle$ for \underline{b}_4 and \underline{b}_5 and with $\underline{b} = a\langle 1\bar{1}0 \rangle$ for b_6 and b_7 . Because the interactions must proceed along the intersection of the planes containing the reactant dislocations, the steps were created and verified in the directions specified in the expressions of 7-1 and 7-2, whereas the discontinuities should be created along $[1\bar{1}0]$ in 9-1 and along $[11\bar{1}]$ in 9-2. The latter directions have not been verified because of the short lengths of the segments.

Energy of interaction

One argument against the possibility of the dislocation dissociation in bcc metals is the frequently observed cross-slip. It is generally believed that this phenomenon signifies that the metal has a very high γ_{SF} . This is not necessarily true for bcc metals as for fcc metals, because of the involved cross-slip processes.

There are two types of cross-slip (80): the so called "easy" and "difficult" cross-slip. The "easy" cross-slip requires no extra energy since there is no change in dislocation energy during the cross-slip process. The "difficult" cross-slip needs an activation energy to initiate the process. For example, to attain the constriction between partials

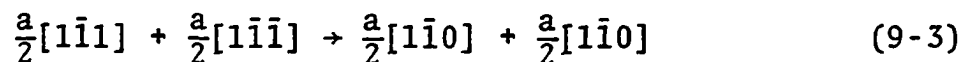
before cross-slip, activation energy is required. Generally, the activation energy for cross-slip comes from the thermal fluctuation and/or the increase in the resolved shear stress.

In the case of Nb, all its $a\langle 100 \rangle$ and $(a/2)\langle 111 \rangle$ dislocations are stable as reported by Head (87). The observed dislocation dissociation in the present study follows the Crussard model. The partials have Burgers vectors $(a/3)\langle 111 \rangle$ and $(a/6)\langle 111 \rangle$ which together give the same type of Burgers vector, $(a/2)\langle 111 \rangle$, for the perfect dislocation. Thus, it is possible for the dislocations to cross-slip without constriction. According to this argument, the cross-slip for dislocation in bcc metals should be more of the "easy" type rather than the "difficult" type, and consequently cross-slip should be easier at room temperature. Since cross-slip occurs readily when there is no energy change, a reduction in energy should cause cross-slip to occur even more readily. An example is shown in Fig. 6. The dislocation with $\underline{b} = (a/2)[\bar{1}\bar{1}1]$ on the (011) plane after interacting with an $(a/2)[\bar{1}11]$ dislocation on the (110) plane, has cross-slipped onto the (110) plane.

Energy calculations have been carried out for interactions 7 and 8. The total self-energy before the interaction is 2.05G, the total self-energy of the product dislocation is 1.18G according to interaction 7 and 0.936G according to interaction 8. Thus a more than 50% reduction in self-energy

is obtained following interaction 8. The strong attractive interaction between the two reactant dislocations of interaction 8 has helped the cross-slip process.

The dislocation interactions observed in Fig. 12 are interpreted as in the 7-1 and -2, 9-1 and -2. This interpretation encounters a seemingly unsurmountable difficulty that 9-1 and 9-2 reactions are energetically prohibited. This type of reaction and its energy problem were mentioned by Bollmann (88). Also, a similar interaction, whereby an $a\langle 110 \rangle$ sessile is produced by two $(a/2)\langle 111 \rangle$ screw dislocations in a repulsive cutting was cited by Ikeno and Furubayashi (44). According to Equation 2, there is an increase of $\Delta E = 0.0343G$ per unit length for reaction 9. Two possible reasons may be cited for the onset of reaction 9 despite its energy unfavorableness. One possibility is the existence of stresses in the crystal to destroy the equilibrium condition. Hence reaction 9 occurred under nonequilibrium conditions. Another possibility is that the reaction was actually more complicated than those indicated in the sense that instead of a perfect $a\langle 110 \rangle$ sessile, the product dislocation is composed of two or more partial sessiles. For instance, reaction 9 could be modified to the form,



which is similar to reaction 12 in Hartley's analysis. Note that interaction 9-3 achieves a reduction in energy with

$\Delta E = -1.01G$ per unit length when the surface energy associated with the stacking fault enclosed between the two partials is excluded. If the second possibility is responsible for the circumvention of the energy difficulty associated with reaction 9, the separation of the partials must have been less than $\sim 50 \text{ \AA}$. Otherwise, the partials and the enclosed stacking faults would have been detected, especially upon the application of the weak-beam technique. Whatever the exact reason for the occurrence of reaction 9 might be, it is important to note that the step segments (Aa, Dd, etc.) are much longer than the corresponding discontinuities (bB, cC, etc.) on the opposite side of the loops in Fig. 12. This is a manifestation that reaction 7 can proceed much more readily and extensively than reaction 9 because the former is energetically favored under equilibrium conditions.

Hartley's analysis should be commented that none of his 12 possible interactions would allow the slip process to continue. All other interactions produce barriers or network, thereby stopping the motion of the active glissile dislocations, except reaction 11 in his paper where the interaction leads to the initiation of fine twins. Hence, Hartley's analysis implies that all but one possible interaction between $(a/2)\langle 111 \rangle \{110\}$ dislocations should denote the slip process. The present observations on Nb tend to militate against such an implication. First of all, an energetically

unfavored interaction has been shown to accommodate another interaction on the opposite side of the loop as observed in Fig. 11. Secondly, even though reaction 8 produces an $a\langle 001 \rangle$ $\{110\}$ barrier, it actually promotes the cross slip of a glissile dislocation as shown by the cross slip of segment A_3b_1 in (011) to Aa in (110) in Fig. 9. Without the cross slip, the segment would have to take an apparently more difficult course of movement in the primary slip plane. It is concluded that interactions between $(a/2)\langle 111 \rangle\{110\}$ dislocations may not necessarily hamper the slip process. Some interactions such as 8 are beneficial to or even necessary for the continuation of the slip process in bcc metals.

Irradiated and Irradiated-Annealed Niobium

Damage structure at the as-irradiated Nb

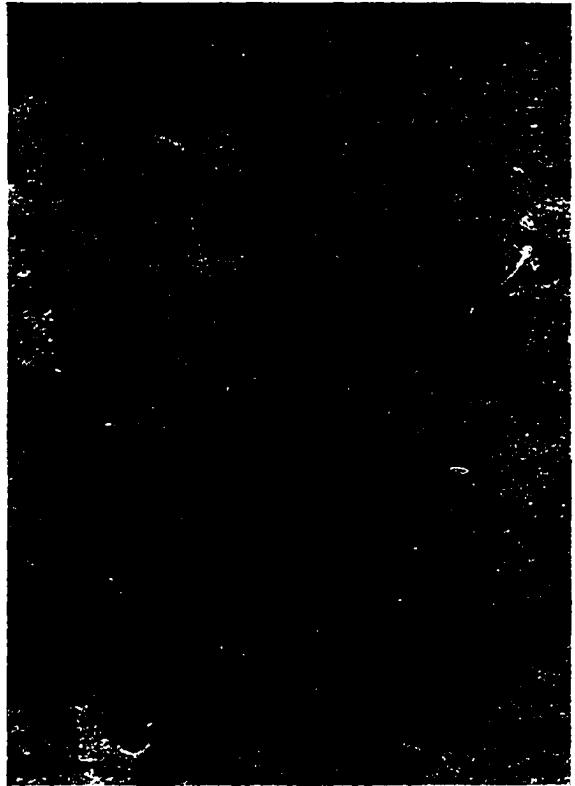
A typical bright-field electron micrograph of the as-irradiated foils is shown in Fig. 15. The striking feature of this micrograph is the coexistence of two types of defect clusters: Small defect clusters (SDC) appear as black spots and large defect clusters (LDC) as dark patches. The SDC have a maximum size of $\sim 100 \text{ \AA}$ and an average diameter (\bar{d}) around 45 \AA , whereas the LDC range from ~ 100 to $\sim 600 \text{ \AA}$ with $\bar{d} = 290 \text{ \AA}$. In addition, SDC differ from LDC in three other aspects. While the images of the SDC are more or less round, those of the LDC are irregular in shape, seldom circular, and change their projected shapes after a large tilting as observed in



Fig. 15. Two types of defect clusters appear in the irradiated lattice of Nb. Large-size dark patches (LDC) represent complex interstitial conglomerates, whereas small-size black spots (SDC) represent vacancy aggregates. Denuded zones are formed along the grain boundary where interstitials are depleted, thus the absence of LDC

Fig. 16a-c. Also, the SDC are fairly uniformly distributed throughout the grains, whereas the LDC appear only in the grain interior, leaving a denuded zone of about 1300 \AA width at the grain boundary. Finally, when viewed under dynamical conditions with nearly zero deviation parameter $w (=s\xi_g)$, where ξ_g is the extinction distance for the \underline{g} reflection), the black spots yielded black-white contrast, as can be seen in the lower left grain in Fig. 15. These black-white contrast images are expected for small dislocation loops lying close to a surface of the foil. Meanwhile, the LDC displayed extremely complex behavior in diffraction contrast under different kinematical conditions. For instance, assuming that they are perfect loops lying on the $\{111\}$ planes with $\underline{b} = (a/2) \langle 111 \rangle$ as those commonly observed in bcc metals (54), no more than 50% of the LDC responded to the $\underline{g} \cdot \underline{b} = 0$ criterion for invisibility. A good example is shown in Fig. 16 where three BF micrographs were taken under three different $\underline{g} = \langle 1\bar{1}0 \rangle$ conditions on a $[111]$ projection. Out of more than 20 LDC, eight responded to the invisibility criterion and became invisible under one of the \underline{g} conditions. The examination of the clusters with the edge-on orientation under a variety of beam directions ($\langle 001 \rangle$, $\langle 011 \rangle$, $\langle 113 \rangle$ and $\langle 133 \rangle$) confirmed that their habit planes are fairly close to $\{111\}$. Fig. 17 illustrates the variation of the image of LDC under four different beam conditions: a) $Z = [001]$ and $g = [110]$. The LDC are

Fig. 16. BF micrographs with $Z = [111]$, and (a) $\underline{g} = [10\bar{1}]$, (b) $\underline{g} = [1\bar{1}0]$, (c) $\underline{g} = [0\bar{1}1]$. The LDC display complex diffraction contrast under different kinematical conditions. The LDC indicated by arrows respond to the $\underline{g} \cdot \underline{b} = 0$ invisibility criterion. Actually no more than 50% of the \overline{LDC} respond to the criterion



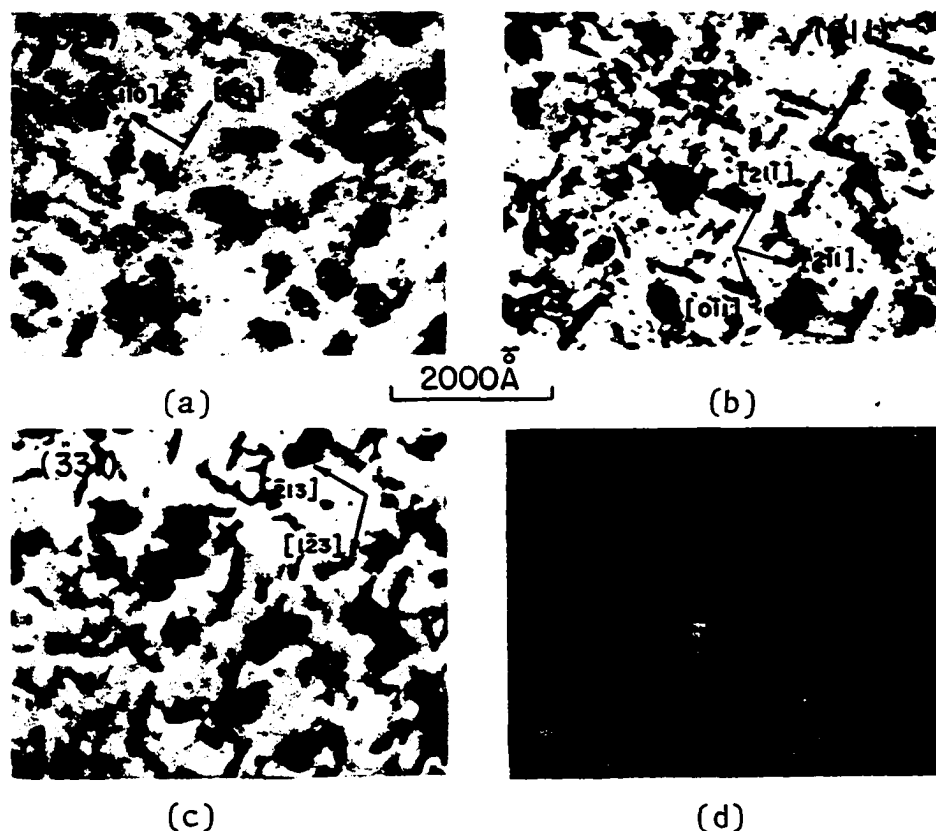
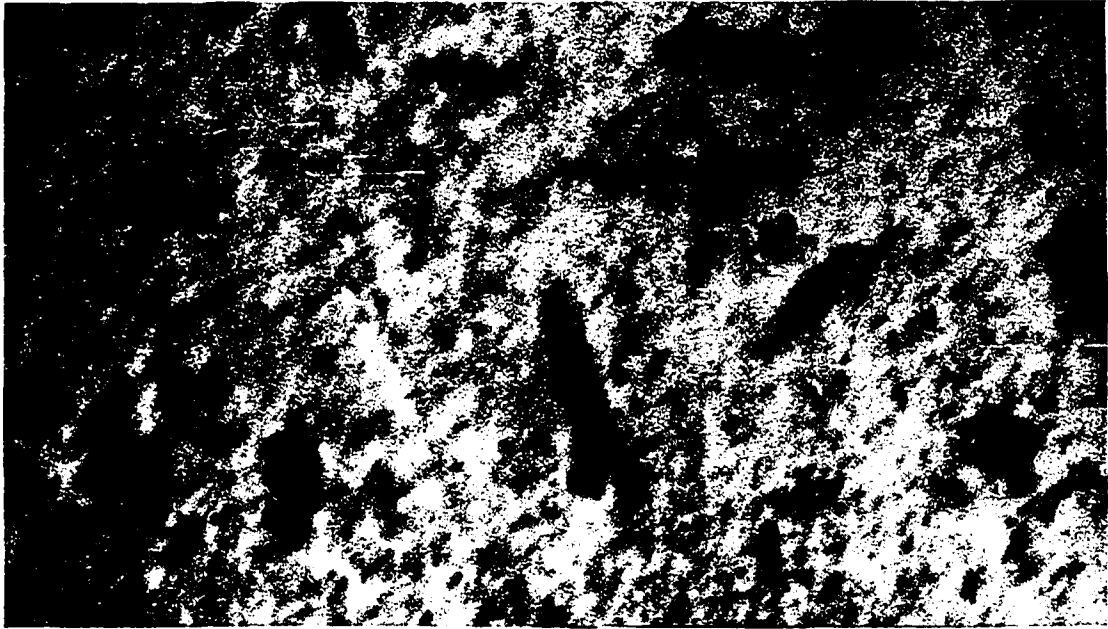


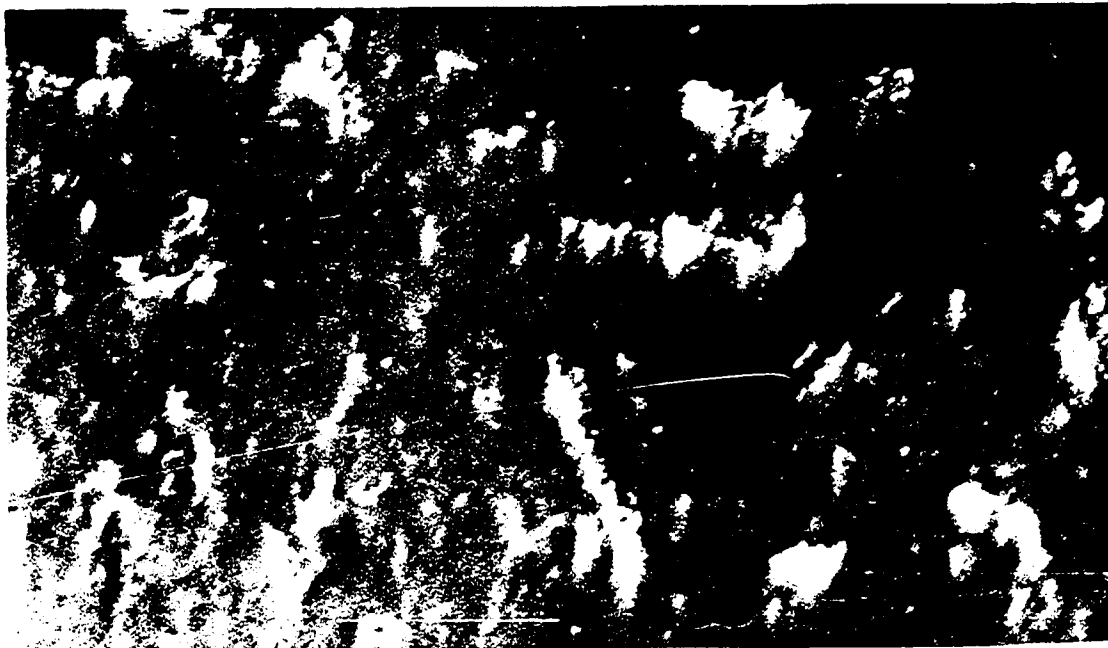
Fig. 17. The diffraction contrast of LDC in the as-irradiated condition under various beam directions. a) $Z = [001]$ and $g = [110]$. Note that LDC are lying parallel to the two $\langle 110 \rangle$ directions and some LDC show fringe contrast. b) $Z = [011]$ and $g = [0\bar{1}1]$. The edge-on LDC are lying along $[21\bar{1}]$ and $[2\bar{1}1]$, which are exactly 90° from $[1\bar{1}1]$ and $[11\bar{1}]$. The other LDC are lying along $[0\bar{1}1]$ on (111) and $(\bar{1}11)$ which are 45° from $[011]$. c) $Z = [331]$ and $g = [\bar{1}10]$. The two planes which are almost edge-on correspond to $(1\bar{1}1)$ and $(\bar{1}11)$. d) $Z = [113]$ and $g = [\bar{1}10]$. LDC A and B are lying parallel to $[\bar{1}10]$ direction, but A is 29.5° and B is 80° away from $[113]$

seen to lie parallel to two $\langle 110 \rangle$ directions with some showing fringe contrast. b) $Z = [011]$ and $g = [0\bar{1}1]$. The edge-on LDC point in the $[2\bar{1}1]$ and $[2\bar{1}\bar{1}]$ directions, which imply the $(1\bar{1}1)$ and $(11\bar{1})$ habit planes, respectively. The other LDC images appear in $[0\bar{1}1]$ on the (111) or $(\bar{1}\bar{1}1)$ plane which is 35.3° from (011) . c) $Z = [331]$ and $g = [\bar{1}10]$. The nearly "edge-on" images correspond to $(1\bar{1}1)$ and $(\bar{1}\bar{1}1)$. d) $Z = [113]$ and $g = [\bar{1}10]$. Two LDC, A and B, are lying parallel to the $[\bar{1}10]$ direction on different planes; A is on $(\bar{1}\bar{1}1)$ and B on (111) . Their images deviate from the edge-on position by 10 and 61° , respectively. This explains why the image's widths are quite different. Figs. 15-17 provide ample evidence to indicate that LDC are not simple loops. Their character is more clearly shown in Fig. 18. Under BF, WBDF and DF conditions, the diffraction contrast of LDC is resolved to display many sub-clusters, which could produce either black or white contrast inside the confines of one LDC as seen in Fig. 18(b). Also observed in Fig. 19 is the dislocation channel where all the LDC and SDC have been removed during a fatigue test at room temperature.

At this point, it is necessary to differentiate the LDC from rafts which have been observed in Mo (57,64,89). Rafts are defined as agglomerates of black spots and/or small loops lying on different layers of one particular $\{111\}$ plane. They are about $60\text{-}100 \text{ \AA}$ thick, $1000\text{-}2000 \text{ \AA}$ in length and width.



(a)



(b)

Fig. 18. The complex characters of the LDC are shown under different image formation processes: $Z = [111]$, (a) BF, $g = [1\bar{1}0]$, (b) WBDF $[2\bar{2}0]$

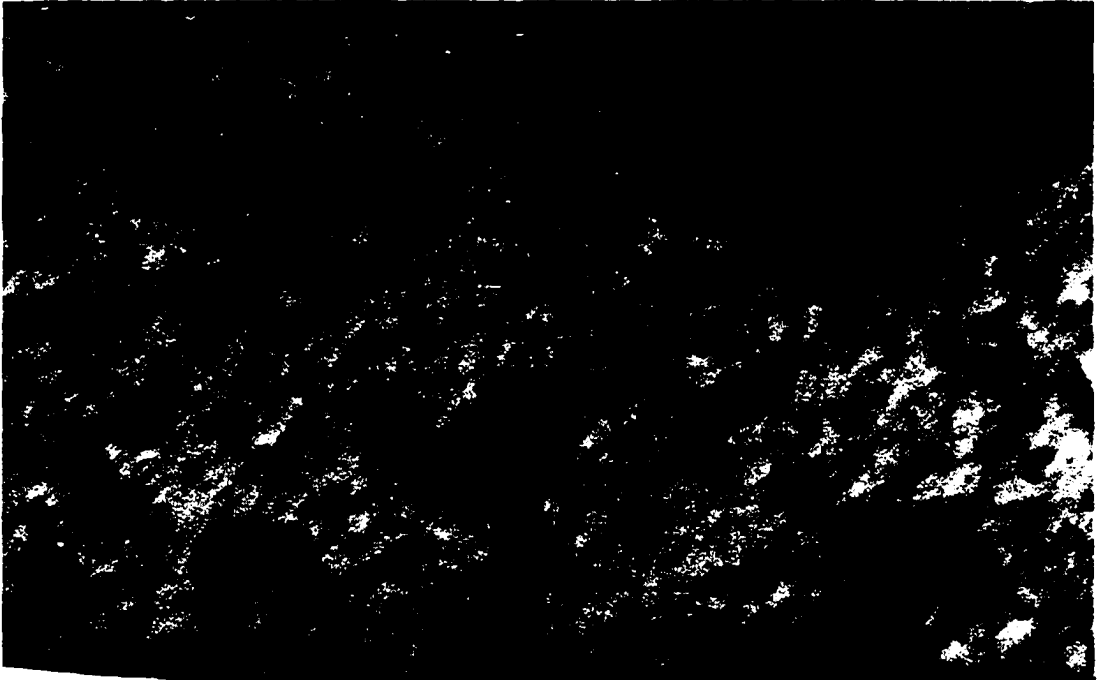


Fig. 18. (Continued) (c) DF, $g = [\bar{1}10]$



Fig. 19. BF micrograph with $Z = [111]$ and $g = [10\bar{1}]$. A dislocation channel was observed after the irradiated specimen had been fatigue-tested

All the structures within a given raft are expected to reveal the same contrast upon imaging the structure under various diffraction conditions. Although LDC also consist of many subclusters and are planar and parallel to the $\langle 111 \rangle$ planes, they are different from rafts in two ways. First, no more than 50% of the LDC can be represented by a single perfect Burgers vector such as $\underline{b} = (a/2)\langle 111 \rangle$, $a\langle 110 \rangle$ and $a\langle 100 \rangle$ as observed in Fig. 16. Second, subclusters within a given LDC display different contrasts with different diffracting conditions as shown in Fig. 18. Thus, LDC are not rafts.

Three more conclusions on the behavior of LDC are worth noting:

- (1) Dislocation channeling occurred in the foils which were heavily decorated with LDC. This observation enables us to rule out the possibility that LDC are precipitates or they involve high concentrations of impurity atoms. In other words, LDC are intrinsic defect clusters.
- (2) The habit planes of the LDC were exactly or close to the $\{111\}$ planes. Besides, the LDC yielded elongated diffraction contrast in one of the three $\langle 110 \rangle$ directions in the (110) projection. Hence, they are considered planar in the sense that their dimensions on the $\{111\}$ planes are much larger than the thickness in the direction normal to the $\{111\}$ planes. However, the thickness is by no means limited to a single interplanar spacing as the simple loops.

(3) The denuded zone of LDC observed along grain boundaries signifies the interstitial nature of the defect clusters.

In addition to these characters in the as-irradiated state, the LDC tended to transform into simple loops upon annealing at intermediate temperatures. An examination of the transformed LDC at 480°C (see part 2, Table 7) indicated that practically all of the LDC in the irradiated foils were of the interstitial type. This revelation coupled with the distinct modes of distribution of LDC and SDC also enable us to identify SDC as of the vacancy type defect clusters. To justify such interpretations, we recall that vacancy loops are thought to be nucleated from collapsed collision cascades (54). Hence it is expected that vacancy clusters will be uniformly generated in the irradiated specimens, in agreement with the observed distribution mode of SDC. Although the nucleation mode of interstitial clusters is not precisely known, doubtless the concentration of interstitials plays a dominant role in the nucleation of LDC, according to Eyre and Bullough (55). Since grain boundaries serve as preferential sinks for interstitials by virtue of the enclosed dislocations, the regions surrounding the grain boundaries would be depleted of interstitials, leading to the formation of the denuded zones observed in Fig. 15.

The different distribution modes between the LDC and SDC require three quantities to describe the number density of

clusters: ρ_L and ρ_{s,r_0} for the LDC and SDC in the grain interior respectively and $\rho_{s,r}$ for the SDC in the denuded zones. The experimental values for the as-irradiated foils are $\rho_L = 3.7 \times 10^{15} \text{ cm}^{-3}$, $\rho_{s,r_0} = 1 \times 10^{16} \text{ cm}^{-3}$ and $\rho_{s,r} = 4.9 \times 10^{16} \text{ cm}^{-3}$. Note the enormous difference between ρ_{s,r_0} and $\rho_{s,r}$, although both quantities deal with defect clusters of the same nature. This difference reflects in part a much more effective recombination process taking place between vacancies and interstitials in the grain interior where the influence of grain boundaries is absent.

Damage structure after annealing

Annealing of the irradiated Nb at temperature from 350°C up caused gradual systematic changes in the defect structure. The changes are best described in terms of the general appearance, size distribution, number density and the l_V/l_I loop ratio.

General appearance The only noticeable change produced by annealing at 350°C is the transformation of a small percentage (<35%) of LDC to simple loops. Four examples of the transformation are marked by arrows in Fig. 20. Otherwise, the defect structure still displays two types of defect clusters with distinct distribution modes. In Fig. 20 the denuded zones again appeared next to the grain boundary on both sides. Annealing at 480°C caused more LDC to transform into simple loops. (See Fig. 21.) The majority of the LDC,



Fig. 20. Annealing at 350°C for one hour was mainly to convert some LDC into simple loops. Four such loops are marked by arrows



Fig. 21. Annealing at 480°C for one hour converted more LDC into simple loops. Numerous complex LDC still remained in the lattice, however



Fig. 22. After one hour annealing at 550°C , the defect structure contained virtually no LDC, only simple loops of vacancies and interstitials

however, still retain their complex appearance. The transformation of LDC suddenly became very effective at 550°C, as evidenced by the virtual disappearance of complex LDC in Fig. 22. Annealing at temperatures above 550°C brought about the following changes in the defect structure:

- (1) The average size of the defect clusters increased steadily from 700°C up (see Figs. 23-25). Annealing below 700°C, however, caused more complicated size changes, which will be described in size distribution.
- (2) The number density of defect clusters decreased progressively.
- (3) The cluster shape became more circular. And
- (4) Relatively long dislocation segments were introduced. (See Figs. 24 and 25.) In this connection, it is worth noting that during the TEM examination of foils annealed at 800-1000°C, many of the dislocation segments were seen to move around, reflecting their glissile character with $\underline{b} = (a/2)\langle 111 \rangle$.

Size distribution The analysis on the size distribution can be made either by counting all clusters together disregarding their nature or by separating vacancy clusters from interstitial ones. The results of the first approach are described here and those of the second approach in the λ_V/λ_I loop ratio section. The data for the overall size distribution are plotted in Fig. 26, where Figure (a) represents the irradiated foils and Figures (b) to (e) refer to foils annealed at five different temperatures. The plots in (a) and (b) feature a sharp, intense peak at 45 and 86 Å, respec-

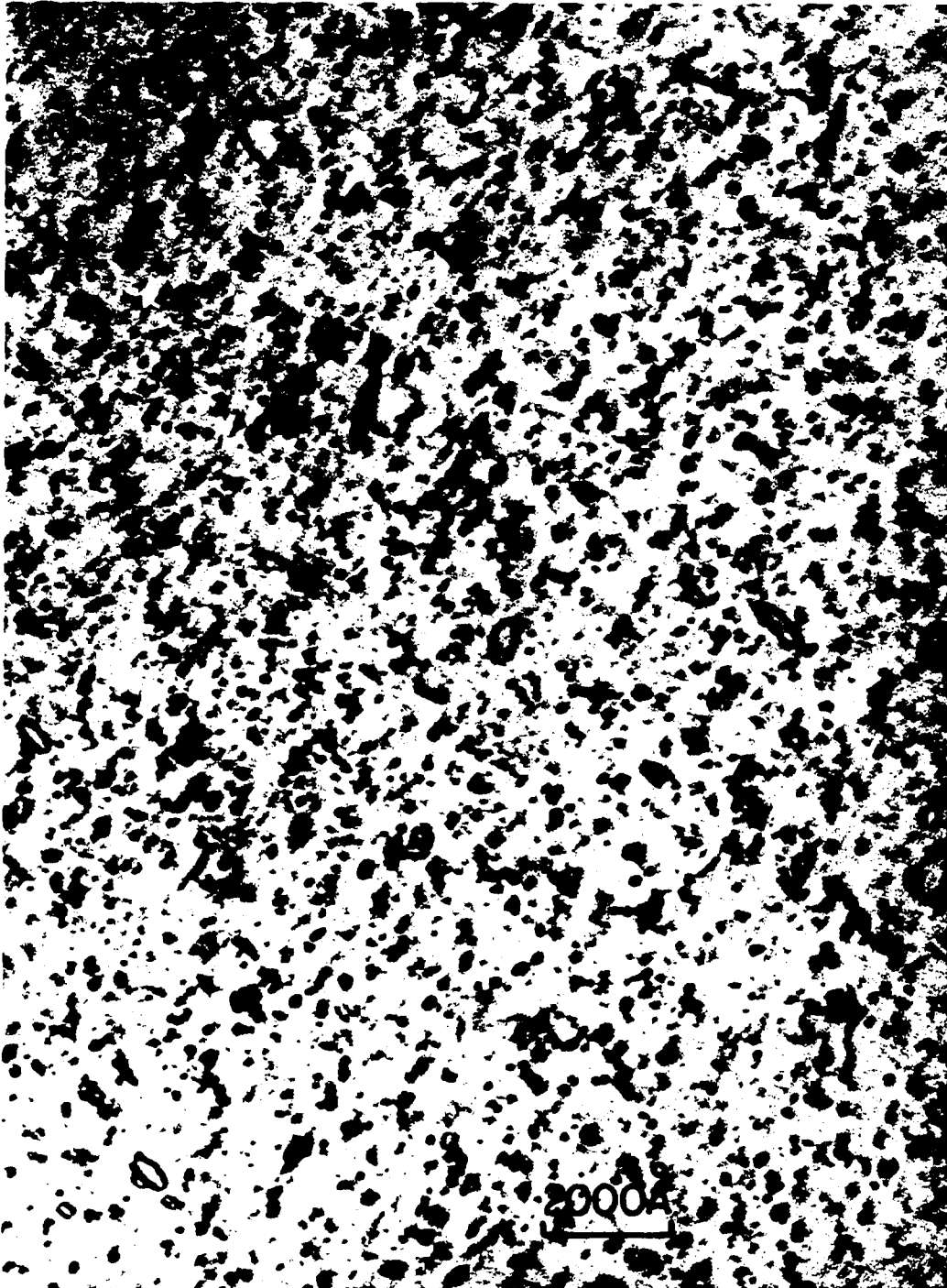


Fig. 23. Annealing at 700°C mainly caused the shrinkage and eventual disappearance of the majority of interstitial loops. Meanwhile, the growth of vacancy loops became prominent

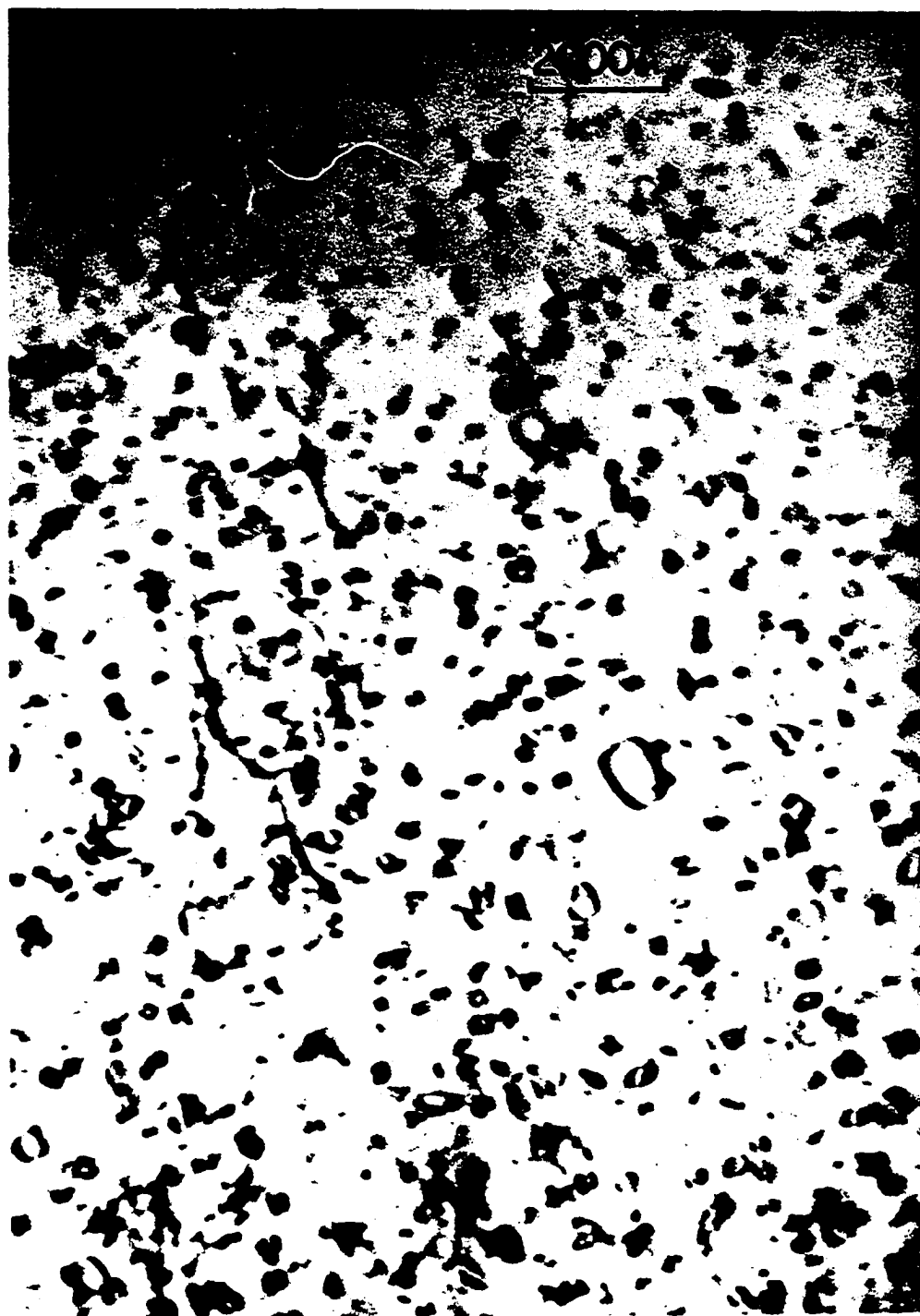


Fig. 24. The defect structure of the irradiated Nb after annealing at 800°C for one hour is composed of both types of loops and also dislocation segments introduced as a result of vacancy-loop coalescence



Fig. 25. A drastic decrease is seen in the number density of loops in specimens annealed at 900°C for one hour. Although vacancy loops dominated the defect structure, many interstitial loops persistently remained

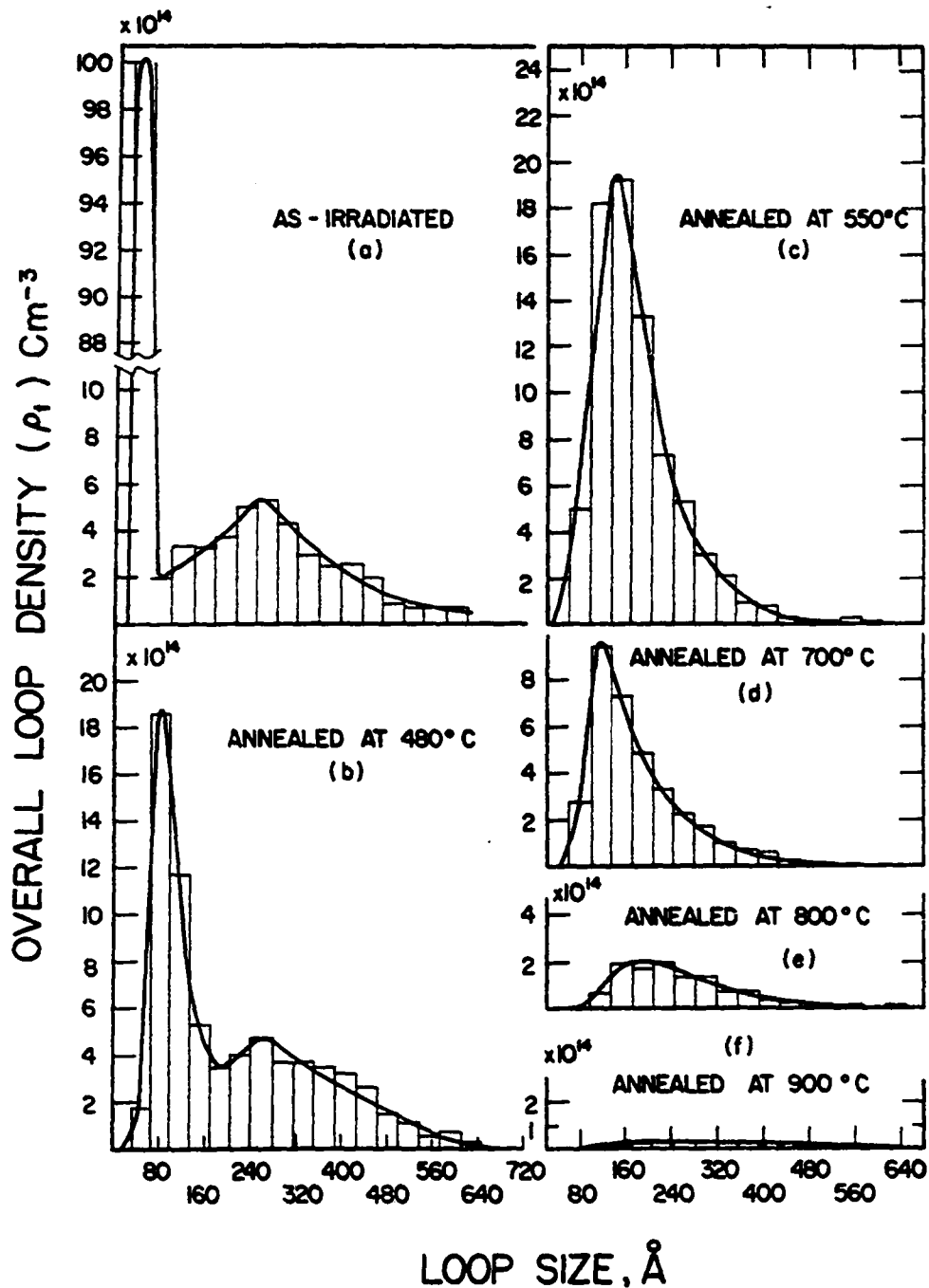


Fig. 26. Histograms and best-fit curves showing the size distribution of defect clusters as a function of annealing temperature T_a . Note the change in the size-distribution spectrum from a two-peak pattern in (a) and (b) to a single-peak pattern for $T_a > 500^\circ\text{C}$ in (c) to (f)

tively, and another smaller peak at 260 \AA . The emergence of two peaks is a manifestation of the coexistence of the SDC and LDC in the defect structure. As T_a exceeded 550°C , the transformation of the LDC became complete. Thus figures (c) and (e) exhibit only one peak which shifted in position first downward to 135 \AA at $T_a = 550^\circ\text{C}$ and to 122 \AA at 700°C , then upward at higher T_a . See data in Table 6. Besides the position shift, the peak is also considerably broadened for $T_a > 800^\circ\text{C}$. The same decrease-increase trend is detected for the average size (\bar{d}) from the data listed in Table 6.

Other data summarized in the table show significant changes in the maximum (d_{max}) and minimum (d_{min}) sizes of clusters. For d_{max} , the coexistence of the LDC and SDC in the irradiated foils requires two values to better express this quantity: 600 \AA for LDC and 100 \AA for SDC. As the LDC were gradually transformed into simple loops in the early stages of annealing, the two-value presentation of d_{max} became impractical. Consequently only single values were obtained for the annealed foils. Based on the enormous difference between the d_{max} values for the LDC and SDC in the irradiated Nb, it is reasonable to assign the value (760 and 840 \AA) of d_{max} at $T_a = 350$ and 480°C to the LDC. At $T_a = 550^\circ\text{C}$, the d_{max} value remained at 840 \AA , indicating that the growth of interstitial clusters has been halted. For $T_a = 700^\circ\text{C}$, there is a steady increase in d_{max} , which is due

Table 6. Data on the overall number density ρ_t and size distribution of defect clusters in irradiated and irradiated-and-annealed niobium

Foil condition	ρ_t, cm^{-3}	Cluster size, \AA				Remarks	
		Average (\bar{d})	Maximum (d_{max})	Minimum (d_{min})	At the distribution peak		
Irradiated	13.7×10^{15a}	LDC-290	LDC-600		LDC-260	$\rho_L = 3.7 \times 10^{15} \text{cm}^{-3}$ $\rho_{S,r_0} = 1.0 \times 10^{16} \text{cm}^{-3}$ $\rho_{S,r} = 4.9 \times 10^{16} \text{cm}^{-3}$	
		SDC-45	SDC-100		SDC-45		
Irr. & ann. at	7.3×10^{15a}	214	LDC-760		LDC-260 SDC-86		
		480	215	LDC-840	LDC-260 SDC-86		
	550	7.7×10^{15}	180	840	135		
	700	3.5×10^{15}	183	1150	~45	122	Coalescence of loops was prominent.
	800	1.2×10^{15}	265	1610	87	190	Dislocation motion observed during TEM examination.

^aThese ρ_t values were obtained by counting the clusters in the grain interior. Hence for the as-irradiated foils, $\rho_t = \rho_L + \rho_{S,r_0}$, where ρ_L and ρ_{S,r_0} are the densities of the LDC and SCD in the grain interior.

Table 6. (Continued)

Foil condition	ρ_t, cm^{-3}	Cluster size, \AA				Remarks
		Average (\bar{d})	Maximum (d_{max})	Minimum (d_{min})	At the distribution peak	
900°C	2.7×10^{14}	436	1800	120	320	
1000	7.2×10^{13}	504	3500	226	400	

largely to the growth of vacancy loops. In fact, no interstitial loops larger than 610 \AA in diameter have been detected in foils annealed above 700°C , at which loops larger than 1000 \AA were found to be exclusively of the vacancy type.

The situation with d_{\min} is simpler because this quantity deals only with the vacancy clusters. The experimental determination of d_{\min} , however, is restricted to values greater than 45 \AA , which is the lower limit of the particle-size analyzer at the magnification of 100,000X. Hence reliable values could be obtained only for $T_a > 700^\circ\text{C}$. The measured values of d_{\min} show steady increases from 45 \AA to 226 \AA as T_a was raised from 700° to 1000°C .

Number density The same two approaches can be used to analyze the effect of post-irradiation annealing on the number density of defect clusters. Again the overall analyses are described here and the separate analyzed in the next section. Partly because of the transformation of the LDC during annealing and partly for the convenience of comparison, we adopted a single quantity, ρ_t , to denote the total overall number density of clusters for the annealed foils and set $\rho_t = \rho_L + \rho_{S,r_0} = 13.7 \times 10^{15} \text{ cm}^{-3}$ for the irradiated Nb. Other experimental values of ρ_t are included in Table 6.

To make further use of the defect-cluster counting, we defined $\rho_t = \sum_i \rho_i$, where i refers to the size range within which certain number of clusters is counted per cm^3 . By

knowing the ρ_i value together with the ℓ_V/ℓ_I loop ratio in the same range, the average size of loops could be fairly accurately determined according to the expression $\bar{d} = \frac{\sum_i \rho_i d_i}{\sum_i \rho_i}$, where d_i is the mid-size of the loops in the i th range. The results of the counting thus conducted are tabulated in Part 1, Table 7. The values given in parentheses are the percentages of ρ_i for a given T_a . Note that 75% of the clusters are smaller than 160 Å in the irradiated foils, whereas large percentages (21, 42, 38 and 52% for $T_a = 480, 550, 700$ and 800°C , respectively) of clusters fall in the size range 160 to 299 Å in the annealed foils. At $T_a = 900^\circ\text{C}$, the defect clusters are about equally distributed in all size ranges greater than 160 Å. These data will also be further used in the analyses described in the following section.

The ℓ_V/ℓ_I loop ratio and the size distribution and number density of vacancy and interstitial loops While the vacancy and interstitial clusters distinguish themselves by their sizes in Figs. 15-19, such a distinction no longer exists after the foils have been annealed for one hour at 550°C and above. Therefore, to determine the ℓ_V/ℓ_I loop ratio in most of the annealed foils, TEM examinations must be conducted on individual loops statistically. Moreover, to attain a reliable determination of the average size of the two types of loops at each T_a , we need to evaluate the ℓ_V/ℓ_I ratio in different size ranges. The analyses were made in this manner

Table 7. Detailed analyses on the λ_V/λ_I loop ratio and number densities of vacancy and interstitial loops in irradiated and irradiated-and-annealed niobium

Part 1. The overall number density (10^{14} cm^{-3}) of defect clusters						
Size	>500	499-400	399-300	299-160	<160	Total (ρ_t)
Irr.	2.16(1.6%)	5.36(3.9%)	9.69(7.1%)	17.07(12.5%)	102.72(75%)	137.00
Irr. & ann. at						
480	3.45(4.8%)	6.66(9.3 %)	9.82(13.7%)	15.30(21.4%)	36.28(51%)	71.51
550	0.53(0.7%)	1.10(1.4%)	4.38(5.7%)	31.72(42%)	38.74(51%)	76.47
700	0.28(0.8%)	0.75(2.2%)	2.52(7.3%)	13.11(38%)	18.01(52%)	34.67
800	0.58(4.8%)	0.73(6.1%)	2.22(18.4%)	6.29(52%)	2.22(18.4%)	12.04
900	0.79(29.5%)	0.57(21.3%)	0.68(25.4%)	0.63(23.5%)	0.01(0.4%)	2.68
Part 2. The λ_V/λ_I ratio of loops larger than 160\AA						
Foil condition	In size range \AA				Total	Normalized total
	>500	499-400	399-300	299-160		
Irr.	a	a	a	a		
Irr. & ann. at						
480°C	0/3	0/5	0/9	3/6	3/23	1/7.7
550	1/6	1/3	3/5	4/7	9/21	1/2.3
700	3/0	8/5	19/9	25/16	55/30	1/0.55
800	7/3	14/7	22/6	30/16	73/32	1/0.44
900	8/1	9/4	24/11	23/9	64/25	1/0.39

^aPresumably all interstitial type.

Table 7. (Continued)

Part 3. Deduced number densities (10^{14} cm^{-3}) of interstitial loops $>160\text{\AA}^b$						
Size	>500	499-400	399-300	299-160	Total	\bar{d} , \AA
Irr.	2.16	5.36	9.69	17.07	34.28	290
Irr. & ann. at						
480°C	3.45	6.66	9.82	10.25	30.18	357
550	0.45	0.83	2.74	20.19	24.21	240
700	0	0.29	0.81	5.12	6.22	243
800	0.17	0.24	0.48	2.19	3.08	287
900	0.09	0.17	0.21	0.18	0.65	371
Part 4. Deduced number densities (10^{14} cm^{-3}) of vacancy loops $>160\text{\AA}^b$						
Size	>500	499-400	399-300	299-160	Total	\bar{d} , \AA
Irr.	0	0	0	0	0	
Irr. & ann. at						
480°C	0	0	0	5.05	5.05	226
550	0.08	0.27	1.64	11.53	13.52	232
700	0.28	0.46	1.71	7.99	10.44	234
800	0.41	0.49	1.74	4.10	6.74	299
900	0.70	0.40	0.47	0.45	2.02	412

^bValues obtained by applying the appropriate loop ratio listed in Part 2 to the overall number densities given in Part 1.

and the results are summarized in Parts 2-4, Table 7. The following results are particularly important in exploring the annealing behavior of the defect clusters:

(1) The normalized ratios of the total vacancy and interstitial loops in the last column of Part 2 reveal the trend that, as the annealing temperature rises, the ratio is shifted more and more towards diminishing interstitials.

(2) Despite this trend, many interstitial loops still persisted in all sizes above $\sim 160 \text{ \AA}$ in the annealed foils with T_a as high as 1000°C . Such persistence of interstitial loops is similar to that observed in neutron-irradiated Mo (57a-c), but in sharp contrast to the rapid disappearance of interstitial loops at temperatures greater than 200°C (0.427m) in neutron-irradiated Cu (90,91).

(3) As might be expected, the interstitial and vacancy loops display quite different annealing behavior. For instance, because the clusters in sizes greater than 160 \AA are interstitial aggregated in the irradiated foils, their total number density $\rho_{t,I}$ was initially at the maximum value of $34.3 \times 10^{14} \text{ cm}^{-3}$. Annealing caused a steady decrease in $\rho_{t,I}$ to 30.2, 24.2, 6.3, 3.1 and $0.65 \times 10^{14} \text{ cm}^{-3}$ at $T_a = 480, 550, 700, 800$ and 900°C , respectively. Meanwhile, since vacancy clusters are predominantly smaller than 100 \AA in diameter in the as-irradiated foils, the initial value of $\rho_{t,v}$ for $d > 160 \text{ \AA}$ is zero. Hence upon annealing, $\rho_{t,v}$ first emerged with a finite

value, reached a maximum of $13.5 \times 10^{14} \text{ cm}^{-3}$ at $T_a = 550^\circ\text{C}$ before finally decreasing at higher T_a . Another difference between the annealing behavior of vacancy and interstitial clusters is that the average size \bar{d} of the interstitial clusters changed rather unsystematically - the deduced value first increased, then decreased and again increased with increasing T_a (see data in Part 3, Table 7).

This unsystematic change is not difficult to explain, if we take a close look at the size distribution of the interstitial loops in part of Table 7. As the specimen condition was changed from as-irradiated to annealed at 480°C , the large ($>300 \text{ \AA}$) and the smaller interstitial cluster densities were seen to undergo an increase and a decrease, respectively. At the same time, the observed value for the d_{max} changed from 600 \AA to 840 \AA and \bar{d} increased from 290 \AA to 357 \AA . These observations resulted from the transformation of multilayered LDC into simple loops. At 550°C , the growth of the interstitial loops ceased because the transformation was completed. Although the d_{max} value remained at 840 \AA , there was a drastic drop in population of large size ($>300 \text{ \AA}$) loops and an increase in density of small sized ($160\text{-}300 \text{ \AA}$) loops, thus causing the remarkable decrease in \bar{d} at the 550°C anneal. In foils annealed above 700°C , the maximum loop size dropped to less than 610 \AA and the total population of loops decreased. However, the density of the large loops decreased at a much

slower pace than the small loops. From Part 3 of Table 7, we note that as the annealing temperature was raised from 550°C to 900°C, about 20% of the large loops ($>500 \text{ \AA}$) survived, but less than 1% of the small loops (160-300 \AA) remained. Thus, the change in size-density distribution is shown to be responsible for the increase in \bar{d} of the interstitial loop in foils annealed above 700°C.

The population of the large vacancy loops, on the other hand, increased progressively with increasing T_a , so did the \bar{d} value of the vacancy loops. To some extent, this behavior of vacancy loops reflects that vacancies are the moving species of point defects during annealing at and above 550°C, thus giving rise to a steady growth of the surviving vacancy loops.

Defect production

Before attempting an explanation of the present results, it is necessary to determine whether our observations are consistent with other studies of the neutron-produced defect structure in Nb. Four other studies, wherein Nb specimens of comparable impurities were irradiated under similar conditions, were selected and their results compared with those of the present study (Table 8). Our result on the $\{111\}$ habit planes of the defect clusters is in agreement with Huber *et al.* (69). Also our experimental value of $\rho_t = 1.37 \times 10^{16} \text{ cm}^{-3}$ falls in the middle of the range 1.4×10^{15} to $9 \times 10^{16} \text{ cm}^{-3}$ covered by three earlier studies (63, 65 and 66). Our measured values for

Table 8. Comparison of TEM observations on the nature, geometry and number density of defect clusters in the irradiated Nb reported by the present and previous workers

Investigators	Irradiation		Impurities, wppm	
	Fluence	$T_i, ^\circ\text{C}$	Substi- tutional	Inter- stitial
Chang & Chen (present)	8×10^{19}	80	1100	260
Agarwal et al. (66, 1976)	9×10^{19}	50	$\sim 340^c$	O_2 -250 O_2 -480
Loomis & Gerber (63, 1973)	4.0×10^{19} 3.4×10^{19}	50	$\sim 340^c$	85 202
Huber et al. (69, 1970)	8×10^{17}	77	ND ^d	ND ^d
Ohr et al. (65, 1970)	2×10^{18}	50	80	104

^aThe interstitial clusters were depleted in zones surrounding the grain boundary.

^bNot determined because of the small size. Possibly lying on $\{111\}$ with $b = (a/2)\langle 111 \rangle$.

^cImpurity contents estimated from vendor's catalog.

^dND = not determined; NR = not reported.

^eEstimated from Fig. 5 of Reference 63.

Defect clusters			
Nature	Geometry	Density, cm^{-3}	$\bar{d}, \text{\AA}$
Interstitial ^a	Lying on {111}, complex \underline{b}	$\rho_L = 3.7 \times 10^{15}$	290
Vacancy	-- ^b	$\rho_{S,r_0} = 1.0 \times 10^{16}$ $\rho_{S,r} = 4.9 \times 10^{16}$	45
ND ^d	ND ^d	5.4×10^{16} 9.0×10^{16}	d_{rms} 60 30
ND ^d	ND ^d	1.4×10^{15e} 6×10^{16e}	
$\ell_V/\ell_I = 1/1.86$ for 250 loops	Lying on {111}, $\underline{b} // \langle 100 \rangle$, $\langle 100 \rangle$, and $\langle 111 \rangle$	$\rho_V = 7 \times 10^{14}$ $\rho_I = 1.3 \times 10^{15}$	NR ^d
"predominantly" interstitial		6.5×10^{15}	82

separate number densities of interstitial and vacancy clusters, however, are more than ten times greater than those (3.7×10^{15} vs 7×10^{14} for ρ_S and $(1.0-4.9) \times 10^{16}$ vs 1.3×10^{15} for ρ_V) given by Huber et al. (69). These differences are not entirely unexpected because the fluence used in the latter work was two orders of magnitude lower than ours. All listed values for the number density of clusters in Table 8 are consistent with the conclusion (57a-c) that the production of defect clusters by neutrons and other energetic particles is highly sensitive to the fluence, irradiation temperature and specimen impurities.

While the number density of defect clusters per se is of primary importance in the assessment of radiation damage, equally important is the number density of vacancies (n_V) or interstitials (n_I) enclosed in the clusters. By comparing n_V or n_I with the number density of displaced atoms n_D calculated from the fluence, the ratio n_V (or n_I)/ n_D signifies the efficiency of cluster production in the specimen under the specified conditions of irradiation. To calculate n_V from the measured values of loop density, we define $n_V = \sum_i N_i n_i$, where N_i is the number density of the vacancy loops in the i th range (at 36 Å interval) of loop size and n_i is the number of vacancies enclosed in each loop. Three assumptions were made to calculate n_i : (1) the loops are round, (2) the thickness of the loops is given by $t = |\underline{b}|$, which is $\sqrt{3}a/2$ for $\underline{b} = (a/2)\langle 111 \rangle$

and (3) the volume occupied by each vacancy is approximately equal to the unrelaxed atomic volume, which is $\Omega = a^3/2$. Consequently we have

$$n_i = \pi d_i^2 t / 4\Omega = \lambda d_i^2 |\underline{b}| / 2a^3, \quad (10)$$

and

$$n_V = \frac{\sqrt{3}\pi}{4a^2} \sum_i N_i d_i^2, \quad (11)$$

for vacancy loops lying on the $\{111\}$ planes with $\underline{b} = (a/2)\langle 111 \rangle$, where d_i is the radius of the loop. Similar formulae were used for calculating the interstitials, n_I , per cm^3 enclosed in all interstitial loops except those designated as LDC, which are not simple loops. The maximum values thus calculated for n_V and n_I from the data for the pertinent loop densities listed in Tables 6 and 7 are 8.4×10^{18} vacancies per cm^3 in the denuded zones of the as-irradiated foils and 5.4×10^{19} interstitials per cm^3 in the foils annealed at 480°C .

The number density of displaced atoms or Frenkel pairs is calculated from the modified Kinchin and Pease model (92) using the formula

$$n_d = (\phi t \cdot n_o \cdot \sigma_d) \cdot (\kappa \hat{E} / 2E_d) \quad (12)$$

where $\phi t = 8 \times 10^{19} n(E > 0.1 \text{ MeV}) / \text{cm}^2$ is the irradiation fluence, $n_o = 5.6 \times 10^{22} \text{ atoms/cm}^3$ is the number density of host atoms, $\sigma_d = 3 \times 10^{-24} \text{ cm}^2$ is the displacement cross section, $\kappa \sim 0.8$ is the displacement efficiency, $E_d = 78 \text{ eV}$ (93) is the displacement threshold energy and \hat{E} the damage energy. For Nb, the mean energy of the primary recoils given for an average

neutron energy of 2 MeV by the standard formulae derived from the conservation laws of energy and momentum is 42 keV, which is much lower than the estimated ionization energy at 93 keV. Hence we may set $E = 42$ keV. The calculated value of n_d is $2.8 \times 10^{21} \text{ cm}^{-3}$, which is 333 and 52 times greater than the calculated n_V and n_I values, respectively. From these results, we conclude that only two percent or less of the point defects can survive after their generation to form defect clusters in Nb irradiated at 80°C. This conclusion is in agreement with previous reports (54,94).

Defect clusters

As far as we can determine, the production of interstitial and vacancy clusters in two distinct size ranges by fast neutrons in Nb is firmly established for the first time in the present study. Even here, we detected some evidence in two early reports (63,66) that the same phenomenon had actually occurred, only to be overlooked. For example, the second and third micrographs in Fig. 1 of Reference (66) and several micrographs (Fig. 3c, e, f, h and i and Fig. 4b and c) in Reference (63) also show the coexistence of defect clusters in two separate size ranges.

Perhaps the most serious discrepancy found in the comparison is connected with the report by Ohr et al. (65), who described the nature of the neutron-induced defect clusters in Nb as "predominantly interstitial". Such predominance did

not occur in this study or in the one conducted by Huber et al. (69) nor is interstitial predominance consistent with the concept that vacancy clusters are nucleated from collapsed collision cascades. Although the collapse of collision cascades may be prevented under certain conditions (e.g., the re-entry of the interstitials on the periphery into the cascade interior can stabilize the cascade, thereby eliminating its collapse), it is doubtful that these conditions would prevail in the Nb specimens of Ohr et al. (65). The report by Ohr et al. differs from the present work in still another respect. They found the denuded zones only after the irradiated Nb had been annealed at 600°C for two hrs, as compared with our consistent observations in the as-irradiated Nb. The reasons for the latter difference are also unknown.

Formation of LDC As has been discussed in the foregoing section, the interstitial nature of the LDC is the reasonable conclusion of the observed channeling effect, the denuded zone and the defect nature of the transformed LDC after the 480°C annealing. The same type of defect structure was reported by Loomis and Gerber (63) on Nb irradiated at 50°C of doses 3×10^{17} to 3.5×10^{19} n/cm². They overlooked the nature of the defects but they clearly showed the effect of the dose and the material purity on the damage structure. In samples which received the same dose, the higher the purity the more distinct was the separation of the LDC and the SDC.

The same tendency existed for samples of the same purity but with higher dose.

Two nucleation mechanisms have been considered for the formation of LDC: 1) localized nucleation, 3) the agglomeration of small loops present in the capture volume of an existing loop. Since the second mechanism has been considered as that for the formation of rafts (89), it will be examined first.

Brimhall and Mastel (89) suggested that loops could move through the lattice by a combination of prismatic glide and self-climb to form the rafts. An idealized edge-on representation of the raft configuration is shown in Fig. 27. The interaction and the capture volume between two prismatic loops lying in parallel planes have been estimated (89) based on the calculation by Foreman and Eshelby (95). The interaction force has no singularity within the capture volume from the existing loop to the other loop except when the loops are concentric or touching. However, some questions remain:

- (1) If the small loops can glide and climb a few hundred angstroms because of the interaction force between the loops, it is difficult to see why the loops will arrange themselves into a higher energy situation shown in Fig. 27, instead of coalescing.
- (2) If the loops involve other Burgers vectors such as those for partials or nonprismatic loops, the possibility of

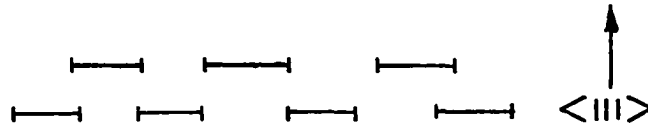


Fig. 27. Idealized representation of an edge-on view of loops contained in a raft

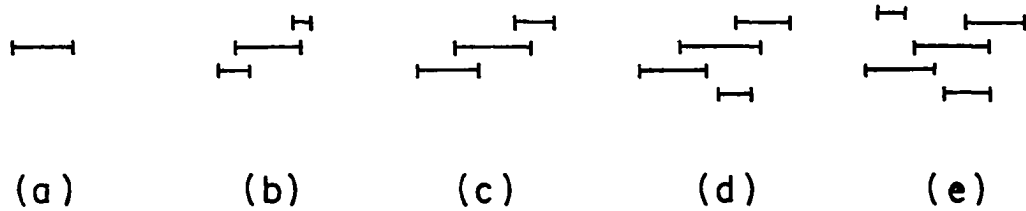


Fig. 28. Illustrates the possibility of nucleation faulted loops in the vicinity of an existing faulted loop. (a) The existing faulted loop. (b)-(e) The progressive formation of other faulted loops, which together constitute an LDC

glide and self-climb becomes small.

(3) The self-climb of loops despite their nature is assumed to occur by short circuit diffusion of atoms around the loop perimeter by a vacancy mechanism (96,57c). The pipe diffusion has an activation energy of 1/2 to 2/3 of that for self-vacancy diffusion. Therefore, interstitial and vacancy loops shall be able to self-climb similarly. If the vacancy loop could exist in a stable size range, such as the vacancy loops in the denuded zone, the interaction between vacancy loops should produce vacancy rafts, which have not been observed.

(4) If every agglomerate of the defect clusters is composed by loops of the same perfect Burgers vector, the complexities of image contrast should not exist. If the loops in the confines of a given agglomerate have different Burgers vectors, then the agglomerate may not be stable.

An alternative mechanism for LDC formation involves localized nucleation of loops within the vicinity of an existing loop. For example, a twinning dislocation with $\underline{b} = (a/6)\langle 111 \rangle$ in the bcc metals is stable if a multilayered fault exists. The stress field of such faulted loop could lead to the nucleation of other faulted loops in the vicinity. The new loops, after growing to a certain size, would in turn nucleate still more loops as shown in Fig. 28.

The LDC thus formed would contain subclusters with the

same Burgers vector, and the subclusters would be arranged according to the nucleation sequence. LDC formed by this mechanism could easily explain the observations that the higher the purity and the dose, the more distinct will be the separation of the LDC and SDC. Hence, in specimens of the same purity level, an increase in dose will enhance the chance for an interstitial cluster to grow past the critical size and to form an LDC. The same explanation can be given to the specimen with lower impurity level of the same dose to have a distinct mode of LDC. Since this mechanism does not involve the prismatic glide and self-climb of small loops but depends on the interstitial diffusion, vacancy LDC are not expected. On the other hand, with the associated faults and the overlapping of the faults of the subclusters, the diffraction contrast of LDC is expected to be complex and will not correspond completely to the invisibility criterion.

Comparing these two mechanisms, the author concludes the localized nucleation mechanism is more plausible than the glide and self-climb mechanism, which imply that the LDC are formed by localized nucleation.

The stacking fault energy γ_{SF} of Nb between the two partials ($(a/6)\langle 111 \rangle$ and $(a/2)\langle 111 \rangle$) has been estimated to be 10 ergs/cm^2 from the results shown in Fig. 3. Such a low value of γ_{SF} tends to strengthen the proposed formation mechanism for LDC, because the existing partial loop can then grow to

the critical size without being transformed into perfect loops. It also promotes the nucleation of partial loops in the vicinity of the existing loop. A detailed model of the proposed mechanism is not available at present, however.

Formation of SDC As mentioned in the foregoing section, SDC represent vacancy clusters and have a density of $1 \times 10^{16}/\text{cm}^3$ inside the grain and $4.9 \times 10^{16}/\text{cm}^3$ in the denuded zone. If we assume that an SDC is a perfect $(a/2)\langle 111 \rangle$ edge loop, then, the total point defects contained in the SDC are only $2.6 \times 10^{18}/\text{cm}^3$, which is one order of magnitude lower than the self-interstitials contained in the LDC. Since grain boundaries and dislocation are preferential sinks for self-interstitials, more vacancies should survive in the as-irradiated specimens. TEM observations revealed the opposite. A reasonable explanation of this discrepancy is that the majority of the surviving vacancies are not detected in the as-irradiated Nb by TEM. This situation can be attributed to the nucleation and growth of the vacancy loops. The vacancy loops are thought to be nucleated from the collapse of the damage cascades. Theoretical calculations (97) indicate that nucleation by co-precipitation of vacancies are too sensitive to the presence of the self-interstitials. Therefore, homogeneous nucleation is not expected for vacancy clusters during irradiation. Indeed, evidence has been reported that Nb specimens electron-bombarded at temperatures from 77°K to 573°K (98)

showed no vacancy loops - only interstitial loops. In the same study, Nb doped with 3000 wt ppm of interstitial impurities and Nb alloyed with 0.15-4.96% Mo also showed no vacancy loop. This is an indication that heterogeneous nucleation of vacancy loops involving interstitial or substitutional impurities is doubtful. There is a general agreement (63,57a) that an increase in interstitial impurities would promote the nucleation of self-interstitial clusters and that an increase in substitutional impurities in Mo tends to decrease the percentage of surviving vacancy loops during post-irradiation annealing. From all these observations, we can conclude that vacancy loops are nucleated from the collapse of the collision cascades.

Since vacancies are probably immobile at the irradiation temperature ($80 \pm 5^\circ\text{C}$) (99,34), we expect that the size of the v-loops is reduced during irradiation because of diffusion of self-interstitials. This is one reason that so many vacancies are stored in the irradiated Nb without being detected by TEM.

Annealing mechanisms

The growth or shrinkage of the dislocation loops during athermal anneal could be attributed to two major processes:

A) Bulk diffusion: Since free self-interstitials start to migrate at 52°K in Nb with $E_{ac} \sim 0.11 \text{ eV}$ (100) most of the surviving self-interstitials are expected to be contained in the interstitial clusters after irradiation. Besides, because of

the high formation energy (~6 eV) of the self-interstitials, their equilibrium concentration during athermal anneal will be negligible. For this reason, it is concluded that diffusion controlled growth and shrinkage will only involve vacancies, not self-interstitials. In this connection, it is important to realize that vacancies are capable of moving with reasonable jump frequency (Γ_V) in Nb at relatively low temperatures because the metal is in a state of nonequilibrium caused by irradiation. Should the metal exist in thermal equilibrium, the jump frequency would have had meaninglessly low values ($2.7 \times 10^{-4} \text{ sec}^{-1}$) at 350°C given by

$$\Gamma_V = Z\nu \exp(-h_V^m/kT), \quad (13)$$

In the calculation, we used Z for the coordination number, $\nu \sim 10^{13}$ for the vibrational frequency and $h_V^m = h_D^b - h_V^f = (4.16^{(90)} - 2.0^{(91)}) \text{ eV} = 2.16 \text{ eV}$ for the activation enthalpy for motion of vacancies. Therefore, we do not expect a strong influence of the vacancy diffusion at this temperature. As the annealing temperature raised to 480, 550 and 700°C, the jump frequencies are 0.3, 5 and 5.4 sec^{-1} , respectively. The latter values are still quite small, nevertheless they are at least meaningful as far as vacancy migration being the annealing mechanism is concerned.

When the annealing temperature exceeded 700°C, the density of large vacancy loops ($>500 \text{ \AA}$) increased while the density of small loops (160-300 \AA) decreased. Also, the d_{\min}

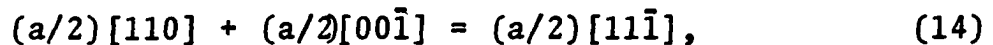
value for vacancy loops increased from 45 Å to 226 Å as the annealing temperature rose from 700°C to 900°C. This is another indication that large loops grow at the expense of small loops. All these results disclose that vacancy diffusion becomes prominent during annealing at temperatures above 500°C.

B) Shear, rotation, glide and self-climb: Since there is no interstitial diffusion after irradiation, the growth of the interstitial loops depends only on the transformation of loops. Thus the density of the large loops was increased, the small loop density and the total loop density were decreased and the number density of enclosed point defects remained constant during annealing below 480°C. Evidently, annealing in the low temperature range is dominated by the transformation of LDC.

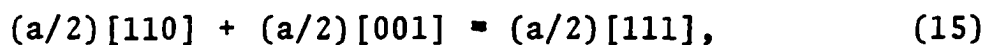
Previous discussion has indicated that the LDC contain subclusters lying on the {111} planes. Without knowing the exact geometry of the subclusters, the process leading to the transformation cannot be specified. It probably involves one or more of the following mechanisms. If we adopt the model proposed by Johnson (101) that an interstitial cluster starts with the formation of diinterstitials from single interstitials in the <110> dumbbell configuration, the primitive form of the subclusters is a single platelet of interstitials lying on a {110} plane. Upon collapsing, the platelet becomes

a small loop with $\underline{b} = (a/2)\langle 110 \rangle$ perpendicular to the loop plane. For a group of $(a/2)\langle 110 \rangle$ loops on different (110) planes to transform into a single loop lying on a $\{111\}$ plane with an appropriate $(a/2)\langle 111 \rangle$ Burgers vector, the following mechanisms are likely to be involved:

- (1) The partial loops with $\underline{b} = (a/2)\langle 110 \rangle$ must be converted to perfect loops with $\underline{b} = (a/2)\langle 111 \rangle$ so as to attain energy stability by eliminating the enclosed stacking faults. To achieve this conversion, Eyre and Bullough (55) proposed the reaction:



through a $[00\bar{1}]$ shear on the (110) plane. Such a reaction per se does not reduce the self-energies of the dislocations involved, but it is made energetically favorable because of the elimination of stacking fault energy. More recently, Jäger and Wilkens (56) examined the alternative reaction,



and concluded that the choice between the two reactions depends on the crystallographic orientation of the specimen surface relative to the (110) loop plane. The chosen reaction will offer a lower total energy in the elastic interaction of the loop with the specimen surface. They have also remarked that reaction 14 or 15 would occur as soon as the loop has reached a critical

radius, which for tungsten is in the range $9 < r_c < 20 \text{ \AA}$.

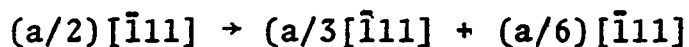
- (2) The next mechanism is for the $(a/2)[111]$ or $(a/2)[11\bar{1}]$ loops to rotate from the (110) planes to the (111) or $(11\bar{1})$ planes, respectively. In so doing, the perfect loop becomes not just prismatic, but also pure edge. According to Eyre and Bullough (55) the driving force for the rotation results from the reduction in elastic energy when the loop character is altered from mixed to pure edge.
- (3) Finally, the prismatic loops can glide to other (111) or $(11\bar{1})$ planes. This mechanism operates under the driving force provided by the elastic interactions between neighboring loops. Through glide together with the supplementary mechanism of self-climb, the multilayered LDC can become a single-layered loop lying on a $\{111\}$ plane with $\underline{b} = (a/2)\langle 111 \rangle$ normal to the loop plane. Eyre and Maher (57c) have analyzed the glide and self-climb mechanism in details under the conditions of post-irradiation annealing.

Whether the transformation of the LDC in the irradiated Nb involves all three mechanisms or only the last one or two mechanisms is still an open question. It is quite possible that the majority of the subclusters have already acquired the $(a/2)\langle 111 \rangle$ Burgers vectors by Mechanism 1 if their sizes had reached the critical radius defined by Jäger and

Wilkins (56). Even the rotation in Mechanism 2 might have taken place in many subclusters during irradiation if the relative orientations of the loop planes to the specimen surface would be favorable. Also important in this consideration are the local conditions of stress and impurities surrounding the subclusters.

SUMMARY

New evidence has been presented for the dissociation of screw dislocation in Nb and for the stacking fault enclosed in the dissociated dislocation. The dissociation followed the Crussard model



on the (211) plane. The stacking fault energy has been calculated from the width of the dissociation to be 10 ergs/cm². Although this value is probably too low in comparison with various estimated values, nevertheless, there are reasons to believe that the observed dissociation of dislocations involves little or no segregation of the interstitial impurities.

Three interactions were observed between two glissile dislocations in the same, or different $\langle 1\bar{1}1 \rangle \{110\}$ slip systems. All three interactions produce sessile dislocations with $b = a\langle 001 \rangle$ or $a\langle 011 \rangle$. Despite the nonslip character of the product dislocation, one interaction, 8, actually promoted cross slip, instead of halting the motion of the reactant dislocation. Also, the occurrence of reaction 9 is somewhat a surprise because it alone would have resulted in an increase in energy unless the product dislocation dissociated into two $(a/2)[110]$ partials. Otherwise, the joint occurrence of reactions 7 and 9 thus demonstrated the inadequacy of the energy requirement when two interactions take place concur-

rently in nonequilibrium conditions under stress.

Neutron irradiation of Nb to the fluence of 8×10^{19} n/cm² ($E > 0.1$ MeV) at 80°C has been shown to produce separate interstitial and vacancy clusters. These two types of clusters differ vastly in size, shape and distribution mode. Small defect clusters are shown to be vacancy clusters which were nucleated from the collapsed collision cascades. Large defect clusters, on the other hand, are interstitial in nature. A possible model of the nucleation of the interstitial cluster is proposed. Annealing of the irradiated Nb at temperature T_a between 350 and 1000°C features three main events. For moderate T_a up to 500°C, annealing is mainly to transform multilayered interstitial clusters into single-layered loops. Between 500 and 700°C, the main event is the shrinkage and eventual disappearance of the majority (~80%) of the interstitial loops. Although the growth of vacancy loops occurs at all T_a , it becomes a main event only when T_a exceeds 700°C. All resolvable loops appear on the {111} planes with $\underline{b} = (a/2) \langle 111 \rangle$ normal to the loop planes, disregarding whether the loops are formed from vacancies or interstitials. Despite the second main event, many interstitial loops persist at T_a as high as 1000°C. The first main event probably involves a maximum of three mechanisms - a $\langle 001 \rangle$ shear, a rotation from {110} to {111} and a combination of glide and self-climb. Meanwhile, the second and the third main events are readily ascribed to the migration of vacancies.

REFERENCES

1. A. S. Nowick and B. S. Berry, "Anelastic Relaxation in Crystalline Solid," Academic Press, New York, N.Y., 1972, p. 225.
2. K. A. Jones and R. M. Rose, *Acta Met.* 24, 45 (1976).
3. S. C. Agarwal, D. I. Potter and A. Taylor, Eighth, Intl. ASTM Symp. on "The Effects of Radiation on Structural Materials," St. Louis, Missouri, May 4-6, 1976.
4. M. G. Ulitchny and R. Gibala, *J. Less Common Metals* 33, 105 (1973).
5. W. Nickerson and C. Altstetter, *Scripta Met.* 7, 229 (1973).
6. J. Diehl, M. Schreiner, S. Staiger and S. Zwiesele, *Scripta Met.* 10, 949 (1976).
7. J. Th. M. de Hosson and A. W. Sleeswyk, *Phys. Status Solidi B* 71, 595 (1975).
8. S. W. Stafford and Rex B. McLellan, *Acta Met.* 22, 1147 (1974).
9. R. D. Heidenreich and W. Shockley, in "Report of a Conference on Strength of Solid," Phys. Society, London, 1948, p. 57.
10. S. Amelincks, "The Direct Observation of Dislocations," Academic Press, New York, 1964.
11. T. B. Massalski, "Alloying Behavior and Effects in Concentrated Solid Solution," Gordon and Breach Science Publishers, New York, 1963, pp. 105-266.
12. *Journal of Microscopy* 98, part 2 (1973).
13. C. P. Chang and C. W. Chen, *Scripta Met.* 9, 369 (1975).
14. C. Wuthrich and W. Frank, "Defects in Refractory Metals," Proceedings of the International Discussion Meeting, held at Mol, Belgium, Sept. 1971, p. 193.
15. G. Taylor, R. Bajaj, and N. Carlson, *Phil. Mag.* 28, 1035 (1973).

16. C. J. Bolton and G. Taylor, *Phil. Mag.* 26, 1359 (1972).
17. J. W. Christian, in "Proceedings of the 2nd International Conference on the Strength of Metals and Alloys," ASM, 1970, p. 31.
18. R. A. Foxall and C. D. Statham, *Acta Met.* 18, 1147 (1970).
19. R. A. Foxall, M. S. Duesbery and P. B. Hirsch, *Can. J. Phys.* 45, 607 (1967).
20. P. B. Hirsch, *Trans. Japan Inst. Metals, Suppl.* 9, 30 (1968).
21. M. S. Duesbery, *Phil. Mag.* 19, 501 (1969).
22. L. J. Teutonico, *Phys. Status Solidi* 14, 457 (1966).
23. R. R. Vandervoort, *Trans. Met. AIME* 245, 2269 (1969).
24. B. Ercaif, G. Fontaine and J. Friedel, *Can. J. Phys.* 45, 481 (1967).
25. M. S. Duesbery, V. Vitek and D. K. Brown, *Proc. Roy. Soc., London*, A332, 85 (1973).
26. R. Chang, *Phil. Mag.* 16, 1021 (1967).
27. V. Vitek, *Crystal Lattice Defects* 5, 1 (1974).
28. H. Eichler and B. Pegel, *Phys. Status Solidi* 35, 333 (1969).
29. J. W. Christian and V. Vitek, *Rep. Prog. Phys.* 33, 307 (1970).
30. M. Yaniaguchi and V. Vitek, *J. Phys. F: Metal Phys.* 3, 523 (1973).
31. A. W. Sleeswyk, *Phil. Mag.* 8, 1467 (1963).
32. A. Fourdeux and A. Berghezan, *J. Inst. Metals* 89, 31 and 191 (1961).
33. R. L. Segall, *Acta Met.* 9, 975 (1961).
34. J. van Landuyt, R. Gevers, and S. Amelinckx, *Phys. Status Solidi* 13, 467 (1966).

35. T. Takeyama and E. J. Koepel, *Phil. Mag.* 8, 2103 (1963).
36. J. Demny, *Phys. Status Solidi* 22, K1 (1967).
37. D. E. Miles, *Proc. Fourth European Regional Conf. on Electron Microscopy*, 1968, p. 419.
38. J. W. Christian, *International Met. Review* 18, 24 (1973).
39. D. A. Smith and K. M. Bowkett, *Phil. Mag.* 18, 1219 (1968).
40. D. A. Smith and J. Gallot, *J. Metal Sci.* 3, 80 (1969).
41. V. Vitek, *Phil. Mag.* 21, 1275 (1970).
42. K. F. Hale and M. H. Brown, *Proc. Roy. Soc., London*, A310, 479 (1969).
43. L. K. France and M. H. Loretto, *Proc. Roy. Soc., London*, A307, 83 (1968).
44. S. Ikeno and E. Furubayashi, *Phys. Status Solidi A* 27, 581 (1975).
45. R. Bullough and A. J. E. Foreman, *Phil. Trans.* A257, 553 (1965).
46. C. S. Hartley, *Phil. Mag.* 14, 7 (1966).
47. A. H. Cottrell, *Trans. Met. Soc. AIME* 212, 192 (1958).
48. V. K. Lindroos, *Phil. Mag.* 22, 637 (1970).
49. V. K. Lindroos and J. K. Kivilahti, *Phil. Mag.* 26, 833 (1972).
50. F. Louchet and L. P. Kubin, *Acta Met.* 23, 17 (1975).
51. R. Priestner and W. C. Leslie, *Phil. Mag.* 11, 895 (1965).
52. C. N. Reid, A. Gilbert and C. T. Hahn, *Acta Met.* 14, 975 (1966).
53. D. Hull, I. D. McIvor and W. S. Owen, *J. Less Common Metals* 4, 409 (1964).
54. B. L. Eyre, *J. Phys. F: Metal Phys.* 3, 422 (1973).

55. B. L. Eyre and R. Bullough, *Phil. Mag.* 12, 31 (1965).
56. W. Jäger and M. Wilkens, *Phys. Status Solidi A* 32, 89 (1975).
- 57a. D. M. Maher and B. L. Eyre, *Phil. Mag.* 23, 439 (1971).
- 57b. D. M. Maher, B. L. Eyre and A. F. Bartlett, *Phil. Mag.* 24, 745 (1971).
- 57c. B. L. Eyre and D. M. Maher, *Phil. Mag.* 24, 767 (1971).
58. K. Niebel and M. Wilkens, *Phys. Status Solidi A* 24, 591 and A 25, 77 (1974).
59. J. D. Elen, Reactor Centrum Nederland Report-96 (1967).
60. R. C. Rau and R. L. Ladd, *J. Nuclear Mater.* 30, 297 (1969).
61. K. Shiraishi, Y. Katano and K. Fukaya, *Crystal Lattice Defects* 6, 51 (1975).
62. R. P. Tucker and M. S. Wechsler, *Radiation Effects* 3, 73 (1970).
63. B. A. Loomis and S. B. Gerber, *Acta Met.* 21, 165 (1973).
64. J. Moteff, D. J. Michel and V. S. Sikka, *Defects and Defect Clusters in bcc Metals and Their Alloys*, *Nuclear Met.* 18, 198 (1973).
65. S. M. Ohr, R. P. Tucker and M. S. Wechsler, *Phys. Status Solidi A* 2, 559 (1970).
66. D. C. Agrawal, E. J. Kramer and B. A. Loomis, *Phil. Mag.* 33, 343 (1975).
67. M. Rühle, F. Haussermann, P. Huber and M. Wilkens, *Proc. 4th European Regional Conf. Electron Microscopy, 1975*, p. 377.
68. R. P. Tucker and S. M. Ohr, *Phil. Mag.* 16, 643 (1967).
69. P. Huber, M. Rühle and M. Wilkens, unpublished work quoted by Wilkens in *Vacancies and Interstitials in Metals*. North-Holland Publishing Co., Amsterdam, 1970, p. 513.
70. L. J. Teutonico, *Acta Met.* 13, 605 (1965),

71. C. S. Hartley, *Acta Met.* 14, 1133 (1966).
72. R. J. Wasilewski, *Scripta Met.* 1, 45 (1967).
73. R. W. K. Honeycombe, *The Plastic Deformation of Metals*, Edward Arnold Co., London, 1968, p. 242.
74. D. J. H. Cockayne, *J. of Microscopy* 98 (2), 116 (1973).
75. P. B. Hirsch, A. Howie, R. B. Nickolson, D. W. Pashley and M. J. Whelan, *Electron Microscopy of Thin Crystals*, Butterworths, London, 1965, p. 265.
76. C. Crussard, *C. r. Acad. Sci., Paris* 252, 273 (1961).
77. P. Humble, *Phys. Status Solidi* 21, 733 (1967).
78. J. P. Hirth and J. Lothe, "Theory of Dislocations," McGraw-Hill Book Co., New York, 1968, p. 346.
79. M. H. Loretto and R. E. Smallman, "Defect Analysis in Electron Microscopy," Chapman and Hall, London, 1975, p. 52.
80. Y. T. Chou, *Scripta Met.* 5, 297 (1971).
81. K. J. Carroll, *J. Appl. Phys.* 36, 3689 (1965).
82. G. Welsch, R. Gibala and T. E. Mitchell, *Acta Met.*, 23, 1461 (1975).
83. A. W. Sleeswyk, "Dislocation Dynamics," *Materials Science and Engineering Series*, McGraw-Hill Book Co., New York, 1968, p. 507.
84. D. N. Seidman and J. J. Burke, *Acta Met.* 22, 1301 (1974).
85. W. T. Reed, Jr., "Dislocations in Crystals," McGraw-Hill Book Co., New York, 1953, p. 69.
86. J. P. Hirth and J. Lothe, "Theory of Dislocation," McGraw-Hill Book Co., New York, 1968, p. 22.
87. A. K. Head, *Phys. Status Solidi* 19, 185 (1967).
88. W. Bollmann, "Crystal Defects and Crystalline Interfaces," Springer-Verlag, Berlin, 1970, p. 77.
89. J. L. Brimhall and B. Mastel, *Radiation Effect.* 3, 203 (1970).

90. M. J. Makin and S. A. Manthorpe, *Phil. Mag.* 8, 1725 (1963).
91. D. E. Barry and B. L. Eyre, *Phil. Mag.* 22, 717 (1970).
92. M. T. Robinson, "Fundamental Aspects of Radiation Damage in Metals" CONF-751006-P1, National Technical Information Service, Springfield, VA, 1975, p. 1.
93. P. Lucasson, "Fundamental Aspects of Radiation Damage in Metals," CONF-751006-P1, National Technical Information Service, Springfield, VA, 1975, p. 42.
94. G. Burger, H. Meissner and W. Schilling, *Phys. Status Solidi* 4, 281 (1964).
95. A. J. E. Foreman and J. D. Eshelby, UKAEA Report AERE R-4100 (1962).
96. C. A. Johnson, *Phil. Mag.* 5, 1255 (1960).
97. K. C. Russell and R. W. Powell, *Acta Met.* 12, 187 (1973).
98. N. Igata, F. Watari and H. Murakami, "Fundamental Aspects of Radiation Damage in Metals," CONF-751006-P1, National Technical Information Service, Springfield, VA, 1975, p. 797.
99. K. Faber, J. Schweikhardt and H. Schultz, *Scripta Met.* 8, 713 (1974).
100. J. Diehl, "Fundamental Aspects of Radiation Damage in Metals," CONF-751006-P1, National Technical Information Service, Springfield, VA, 1975, p. 663.
101. R. A. Johnson, *Phys. Rev.* 134, A 1329 (1964).

ACKNOWLEDGMENTS

I would like to sincerely thank my advisor, Dr. C. W. Chen for his professional guidance and sustaining encouragement throughout the investigation and his help in the preparation of this manuscript. Much gratitude is due Dr. T. E. Scott for his helpful discussions. Also, many thanks to Mr. F. A. Schmidt for his advice and for the preparation of several samples. The experimental work could not have been carried out without the technical assistance of Wayne Buttry, Les Reed and members of the ALRR facility. I wish to express my appreciation to many members of the Chemical Analyses group and the Graphic Arts Department of the Ames Laboratory. The experience and the expertise provided by Miss Verna Thompson in typing this manuscript is greatly appreciated.

Finally, I would like to express my deepest thanks to my parents for their encouragement, and to my wife, Yu-fen, for her patience and understanding throughout my long stay at the Iowa State University.